

ExELS: an exoplanet legacy science proposal for the ESA *Euclid* mission – I. Cold exoplanets

M. T. Penny,^{1,2,3} E. Kerins,^{1,2}★ N. Rattenbury,² J.-P. Beaulieu,^{1,4} A. C. Robin,⁵
S. Mao,^{1,2,6} V. Batista,^{1,3} S. Calchi Novati,^{1,7,8} A. Cassan,^{1,4} P. Fouqué,^{1,9}
I. McDonald,^{1,2} J. B. Marquette,^{1,4} P. Tisserand^{1,10} and M. R. Zapatero Osorio^{1,11}

¹The *Euclid* Exoplanet Science Working Group

²Jodrell Bank Centre for Astrophysics, School of Physics & Astronomy, University of Manchester, Oxford Road, Manchester M13 9PL, UK

³Department of Astronomy, Ohio State University, 140 W. 18th Ave, Columbus, OH 43210, USA

⁴Institut d'Astrophysique de Paris, Université Pierre et Marie Curie, CNRS UMR7095, 98bis Boulevard Arago, F-75014 Paris, France

⁵Institut Utinam, CNRS UMR6213, Université de Franche-Comté, Observatoire de Besançon, Besançon, France

⁶National Astronomical Observatories, Chinese Academy of Sciences, A20 Datun Road, Chaoyang District, Beijing 100012, China

⁷Dipartimento di Fisica 'E. R. Caianiello', Università di Salerno, Via Ponte don Melillo, I-84084 Fisciano (SA), Italy

⁸Istituto Internazionale per gli Alti Studi Scientifici (IIASS), I-84019 Vietri Sul Mare (SA), Italy

⁹IRAP, CNRS – Université de Toulouse, 14 av. E. Belin, F-31400 Toulouse, France

¹⁰Research School of Astronomy and Astrophysics, Australian National University, Cotter Rd, Weston Creek, ACT 2611, Australia

¹¹Centro de Astrobiología (CSIC-INTA), Crta. Ajalvir km 4, E-28850 Torrejón de Ardoz, Madrid, Spain

Accepted 2013 May 24. Received 2013 May 20; in original form 2012 June 20

ABSTRACT

The *Euclid* mission is the second M-class mission of the ESA Cosmic Vision programme, with the principal science goal of studying dark energy through observations of weak lensing and baryon acoustic oscillations. *Euclid* is also expected to undertake additional Legacy Science programmes. One such proposal is the Exoplanet Euclid Legacy Survey (ExELS) which will be the first survey able to measure the abundance of exoplanets down to Earth mass for host separations from ~ 1 au out to the free-floating (unbound) regime. The cold and free-floating exoplanet regimes represent a crucial discovery space for testing planet formation theories. ExELS will use the gravitational microlensing technique and will detect 1000 microlensing events per month over 1.6 deg^2 of the Galactic bulge. We assess how many of these events will have detectable planetary signatures using a detailed multiwavelength microlensing simulator – the Manchester–Besançon microLensing Simulator (MAB μ LS) – which incorporates the Besançon Galactic model with 3D extinction. MAB μ LS is the first theoretical simulation of microlensing to treat the effects of point spread function (PSF) blending self-consistently with the underlying Galactic model. We use MAB μ LS, together with current numerical models for the *Euclid* PSFs, to explore a number of designs and de-scope options for ExELS, including the exoplanet yield as a function of filter choice and slewing time, and the effect of systematic photometry errors. Using conservative extrapolations of current empirical exoplanet mass functions determined from ground-based microlensing and radial velocity surveys, ExELS can expect to detect a few hundred cold exoplanets around mainly G-, K- and M-type stellar hosts, including ~ 45 Earth-mass planets and ~ 6 Mars-mass planets for an observing programme totalling 10 months. ExELS will be capable of measuring the cold exoplanet mass function down to Earth mass or below, with orbital separations ranging from ~ 1 au out to infinity (i.e. the free-floating regime). Recent ground-based microlensing measurements indicate a significant population of free-floating Jupiters, in which case ExELS will detect hundreds of free-floating planets. ExELS will also be sensitive to hot exoplanets

★ E-mail: Eamonn.Kerins@manchester.ac.uk

and sub-stellar companions through their transit signatures and this is explored in a companion paper.

Key words: gravitational lensing; micro – planets and satellites; detection – stars; low-mass – planetary systems – Galaxy: bulge.

1 INTRODUCTION

The discovery of exoplanetary systems is accelerating rapidly with over 860 exoplanets confirmed from ground- and space-based observations¹ and another ~ 2700 candidates detected with the *Kepler* space telescope (Batalha et al. 2013). This is providing a wealth of knowledge on the distribution function of, primarily, hot exoplanets at host separations of $\lesssim 1$ au around FGK-type stars. Recent observations by the *Kepler* space-based transit mission indicate that low-mass exoplanets appear to be common and that around 20 per cent of stellar hosts have multiple planets orbiting them (Batalha et al. 2013). Results from eight years of observations by the High Accuracy Radial Velocity Planet Searcher (HARPS) team (Mayor et al. 2011) indicate that half of solar-type stars host planets with orbital periods below 100 d. The frequency of exoplanets in the super-Earth to Neptune (SEN) mass range shows a sharp increase with declining mass and no preference for host-star metallicity. HARPS also finds that most SEN planets belong to multiple exoplanet systems. An analysis by HARPS of its M-dwarf star sample (Bonfils et al. 2013) indicates that low-mass exoplanets are also common around low-mass stars and that the fraction η of M-dwarf host stars with habitable planets is remarkably high at $\eta = 0.41^{+0.54}_{-0.13}$.

The vast majority of low-mass exoplanet detections to date are ‘hot’, involving planets within ~ 1 au of their host star. Currently only eight ‘cool’ exoplanets have been detected with masses below $30 M_{\oplus}$ and host separations above 1 au. This reflects the fact that such exoplanets are highly demanding targets for both the transit and radial velocity (RV) detection methods, techniques which dominate current exoplanet statistics.

Mapping the cold exoplanet regime is crucial for testing and informing leading theories of planet formation, such as the core accretion and disc instability scenarios. In the core accretion scenario (Safronov 1969; Mizuno 1980; Lissauer 1987), planets form out of a thick disc of gas and dust by the gradual build up of material from dust grains into larger objects through collisions. Once the objects become large enough, they begin to accrete dust and gas via gravity. In the core accretion model, terrestrial planets can be considered as the cores of planets that fail to reach the mass required for runaway gas accretion, either due to their location in the disc or the influence of other planets nearby that grow more rapidly. The core accretion process is most efficient in a region of enhanced disc density where water and other hydrogen compounds condense to form ice (Hayashi 1981; Stevenson & Lunine 1988). This region (the so-called ice or snow line) lies at orbital radii ~ 2.7 au, likely with only a weak host-mass dependence, and is thought to be where most planets form. In the disc instability scenario (Kuiper 1951; Cameron 1978; Boss 1997), giant planets form through a gravitational instability in a gaseous disc. Disc instability may be the only mechanism by which giant planets can form (Boss 2011), whilst terrestrial planets are still thought to form through a process similar to core accretion (Boss 2006). Migration of planets during

formation, due to interactions with the disc, can cause both inward (Goldreich & Tremaine 1980; Ward 1997) and outward migration (Masset & Snellgrove 2001). More violent planet–planet interactions may result in planets being scattered inwards (Nagasawa, Ida & Bessho 2008), outwards or even being ejected completely from their systems (Veras, Crepp & Ford 2009). Tentative evidence of unbound (free-floating) planetary-mass objects suggests that more than one Jupiter-mass planet per star may be ejected in this way (Sumi et al. 2011).

Of the relatively few cool low-mass exoplanets detected to date at host separations above 1 au and mass below $30 M_{\oplus}$, half have been found using the gravitational microlensing technique (Mao & Paczyński 1991; Gould & Loeb 1992). The peak sensitivity of microlensing occurs around the location of the snow line, making it a particularly powerful probe of planet formation. It is also sensitive to free-floating planets whose existence may provide an additional ‘smoking-gun’ signature of the planet formation process.

Whilst all microlensing surveys to date have been ground based, a survey conducted from space is needed to truly open up the cold exoplanet parameter space. The probability of a detectable planetary signal and its duration both scale as proportional to $\sqrt{M_p}$, but given the optimum alignment planetary signals from low-mass planets are still quite strong. The lower mass limit for planets to be detectable via microlensing is reached when the planetary Einstein radius becomes smaller than the projected radius of the source star (Bennett & Rhie 1996). The $\sim 5.5 M_{\oplus}$ planet detected by Beaulieu et al. (2006) is near this limit for a giant source star, but most microlensing events have G- or K-dwarf source stars with radii that are at least 10 times smaller than this. In order to extend the sensitivity to Earth mass and below, it is critical to be able to monitor these small source stars that are unresolved from the ground. The ideal machine is a wide-field imager in space with sub-arcsecond imaging capability.

The advantages of undertaking a microlensing exoplanet survey from space (also discussed in Section 3) were first highlighted some time ago by the study of Bennett & Rhie (2002) who looked at the potential science from the *Survey for Terrestrial Exoplanets* and *Galactic Exoplanet Survey Telescope* mission proposals. Building on these proposals, the *Microlensing Planet Finder* was proposed to the NASA Discovery Programme in 2006 (Bennett et al. 2010a). Having realized the synergies between the requirements for cosmic shear measurement and microlensing planet hunting, a microlensing programme was proposed as an additional survey as part of the Legacy Science of the *Dark UNiverse Explorer (DUNE)* submitted to ESA Cosmic Vision in 2007 (Refregier 2009; Refregier et al. 2010). Ever since, dark energy and microlensing have been advocated for in a joint mission with white papers (Beaulieu et al. 2008) and at international conferences and within the community (Beaulieu et al. 2010, 2011). Our objective is to do a full statistical census of exoplanets down to the mass of Mars from free floating to the habitable zone in complements to the census from the *Kepler* mission. *DUNE* got rebranded into *Euclid* and has been selected as the ESA M2 mission in 2011 October, with a statistical census on exoplanets via microlensing being part of the proposed additional survey in the legacy science.

¹ As of 2013 April. See the Extrasolar Planets Encyclopaedia: <http://exoplanet.eu/>.

The idea promoted in Europe since 2006 of using a single space telescope to conduct both a weak-lensing dark energy survey and an exoplanet microlensing survey was also followed up in the US in a number of white papers and conferences (Bennett et al. 2009, 2010a; Gaudi et al. 2009). In US, the Exoplanet Task Force report (Lunine et al. 2008) to the Astronomy and Astrophysics Advisory committee concluded that ‘Space-based microlensing is the optimal approach to providing a true statistical census of planetary systems in the Galaxy, over a range of likely semimajor axes’. Following this, the US Astronomy 2010 Decadal Survey endorsed a combined approach when it top ranked Wide-Field Infrared Survey Telescope (*WFIRST*; Blandford et al. 2010; Barry et al. 2011; Green et al. 2011, 2012; Dressler et al. 2012). The subsequent report on implementing recommendations of the Decadal Review (Spergel et al. 2012) acknowledges that *Euclid* is also capable of undertaking an exoplanet microlensing survey.

Whilst dark energy studies represent the core science of *Euclid* it also aims to undertake other legacy science. The possibility of an exoplanet survey is mentioned explicitly in the *Euclid* Red Book (Laureijs et al. 2011) and is currently under study by the Euclid Exoplanets Working Group. This paper presents a baseline design for the Exoplanet Euclid Legacy Survey (ExELS). The design for ExELS is being developed using a detailed microlensing simulator, Manchester–Besançon microLensing Simulator (MAB μ LS), which is also presented in this paper. We focus our attention in the present study exclusively on how ExELS will probe the cold exoplanet population through microlensing, but ExELS will also be able to detect hot exoplanets and sub-stellar objects through their transit signatures. This hot exoplanet science is explored separately in a companion paper (McDonald et al., in preparation, hereafter referred to as Paper II). ExELS will be the first exoplanet survey designed to probe exoplanets over all host separations, including planets no longer bound to their host. ExELS will provide an unparalleled homogeneous data set to study exoplanet demographics and to inform planet formation theories.

We begin the paper by outlining the conservative approach we take to our estimates. In Section 3 of this study, we overview the basic theory behind exoplanet detection with microlensing and we also describe the *Euclid* mission and its primary science objectives. In Section 4, we introduce our microlensing simulator (MAB μ LS), we describe the Besançon population synthesis model Galaxy used to generate artificial microlensing events, and we also outline a baseline design for ExELS. Section 5 presents the results of a simulation of the baseline design for ExELS and Section 6 considers the effects of a number of variations and de-scope options to the baseline design. We end with the summary discussion in Section 7.

2 A CONSERVATIVE APPROACH

Throughout our study of the capability of *Euclid* for detecting exoplanets, we adopt a conservative approach. There are two reasons for this. First, the design of *Euclid* is itself still evolving. Secondly, since time on a space telescope is expensive, a feasibility study such as carried out in this paper must demonstrate that key science goals are likely to be achieved rather than merely being an aspiration.

This means that, wherever possible, we aim to make detailed predictions anchored to models which are known to agree with current data. Where details of models require some assumptions, these assumptions must not be overly optimistic. An example of this approach is our simulation of photometry. The most accurate representation of the photometric methods that will be used on the real data would be to simulate point spread function (PSF) fitting or

weighted aperture photometry. However, crowded field photometry is notoriously difficult, and there will always be cases where automated data analysis pipelines will fail to perform the photometry optimally. Simulating all the possible complications in the photometry is impossible. If we were to simulate PSF fitting or weighted aperture photometry, complications that degrade or destroy the photometry would not be modelled, and the assumption we had made, while being accurate, would be optimistic. Instead, we choose to simulate the photometry as unweighted aperture photometry (see Section 4.5 for full details). Aperture photometry is a less accurate representation of the actual data analysis methods that will be used, and is less effective than optimal photometry by a small but sometimes significant amount. However, this choice is conservative and helps to ensure that we do not overpredict the performance of the mission.

Given our conservative approach, we can have confidence that the scientific yields we predict are realizable with *Euclid*.

3 EXOPLANETARY MICROLENSING FROM SPACE

Gravitational microlensing describes the transient deflection and distortion of starlight on milliarcsecond scales by intervening stars, stellar remnants or planets (for a recent review see Mao 2008). Microlensing is distinguished from ordinary gravitational lensing in that whilst multiple images are produced, they are not resolvable. Instead, one observes a single apparent source which appears magnified by a factor

$$A = \frac{u^2 + 2}{u\sqrt{u^2 + 4}}, \quad (1)$$

where the impact parameter u is a dimensionless angular separation between the lens and source measured in units of the angular Einstein radius of the lens. A microlensing event is observable as a transient achromatic brightening of a background source star lasting for $t_E \sim 6\text{--}60$ d, where t_E is the Einstein radius crossing time. For a single lens the light-curve profile is time-symmetric, with a peak magnification occurring when the impact parameter is at its minimum $u = u_0$. The lensing signal from foreground stars is detectable in a few out of every million background stars located in crowded stellar fields such as the Galactic bulge. A planet orbiting a foreground lensing star may, in a few per cent of microlensing events, perturb the microlensing signal causing a brief deviation which lasts for $t_p \sim t_E \sqrt{M_p/M_*}$, where M_* and M_p are the host and planet masses. Typically, t_p is in the region of a day for a Jupiter-mass planet down to a few hours for Earth-mass planets. The intrinsically very low probability $\sim \mathcal{O}(10^{-8})$ of an exoplanetary microlensing signature against a random background source star, coupled with the brief deviation time-scale associated with Earth-mass planets, places huge technical demands on microlensing surveys.

The probability of a planetary perturbation occurring scales roughly as the square root of the planet mass, or more strictly, as the square root of the planet–host mass ratio q (Gould & Loeb 1992). This shallow sensitivity curve makes microlensing ideal for detecting low-mass planets. The scaling breaks down below about a Mars mass, where finite-source effects begin to wash out planetary signatures, even for main-sequence source stars (Bennett & Rhie 2002).

The sensitivity of microlensing to planets peaks close to the Einstein radius r_E with projected semimajor axis $a_{\perp} \sim r_E \sim 2$ au, corresponding to where the microlensing images are most likely to be perturbed (Wambsganss 1997; Griest & Safizadeh 1998).

However, there is significant sensitivity to planetary orbits with $a_{\perp} \sim 0.5$ au, and outwards to infinity (i.e. free-floating planets; Han et al. 2004; Sumi et al. 2011).

Owing to its high stellar density and microlensing optical depth, the Galactic bulge is the best target for microlensing studies. Towards the bulge, extinction is a significant problem at optical wavelengths. Additionally, the extreme stellar crowding and arcsecond-scale seeing mean that only the giant star population can be properly resolved from the ground (Bennett 2004). Observing in the near-infrared lessens the effects of dust and so provides a larger microlensing optical depth (Kerins, Robin & Marshall 2009), but, from the ground, stellar crowding problems are even more severe and noise levels are enhanced due to both the sky and unresolved stellar backgrounds. Therefore, in order to monitor enough source stars, ground-based surveys must regularly cover $\sim 100 \text{ deg}^2$. Current and future ground-based surveys – e.g. Microlensing Observations in Astrophysics (MOA-II; Sumi 2010), Optical Gravitational Lensing Experiment (OGLE-IV; Udalski 2011), Korean Microlensing Telescope Network (KMTNet; Kim et al. 2010) and Antarctic Schmidt Telescopes (AST3; Yuan et al. 2010) – with wide-field imagers will achieve suitable cadence and areal coverage to detect routinely large numbers of giant planets if they exist in sufficient abundance. However, they will not be able to monitor enough stars at high cadence to detect Earth-mass planets at a significant rate. For this reason, targeted follow-up of promising microlensing events by large networks of small telescopes is currently used to achieve high cadence and continuous event coverage (see, e.g., Gould et al. 2010) and to push the sensitivity of ground-based microlensing firmly into the super-Earth regime (Beaulieu et al. 2006; Bennett et al. 2008). However, the follow-up networks only have the capacity to observe ~ 100 events per year or fewer with sufficient cadence (Peale 2003). This allows the mass function to be probed down to $\sim 5\text{--}10 M_{\oplus}$, and possibly the semimajor axis distribution of planets above $\sim 50 M_{\oplus}$, but is unlikely to provide more than isolated detections below these masses (Peale 2003; Bennett 2004; Dominik 2011).

Observations from space are able to overcome many of the problems facing ground-based observers. A space telescope has better resolution due to the lack of atmosphere and also a lower sky background, especially in the infrared. This means that with appropriate instrumentation, a space telescope can resolve main-sequence sources in the bulge and monitor the required $\sim 10^8$ sources over a much smaller area. This in turn allows high-cadence observations on a small number of fields (Bennett & Rhie 2002; Bennett 2004). The fundamental requirement of a space telescope for a microlensing survey is a wide field of view ($\gtrsim 0.5 \text{ deg}^2$), with a small pixel scale. In order to minimize the effect of extinction towards the Galactic bulge, it should observe in the near-infrared. The telescope must also have a large enough collecting area to allow high-precision photometry of main-sequence bulge stars in short exposure times. These are almost exactly the same requirements as for dark energy studies using weak lensing, which are already driving the hardware design of *Euclid*.

3.1 The *Euclid* mission

Euclid is an M-class mission within the ESA Cosmic Vision programme. It aims to investigate the nature of dark energy through measurements of weak gravitational lensing and baryon acoustic oscillations (Laureijs et al. 2011). *Euclid* will comprise a 1.2 m Korsch telescope with a high-resolution optical imager (VIS) and a near-infrared imaging spectrometer (NISP), operating simultaneously. The core science mission will involve a $15\,000 \text{ deg}^2$ wide

survey and 40 deg^2 deep survey over six years to measure galaxy shapes and photometric and spectroscopic redshifts. VIS will observe with a wide optical bandpass covering *R*, *I* and *Z*, and NISP will have available three infrared filters: *Y*, *J* and *H*. The currently envisaged step and stare survey strategy of *Euclid* means that for up to two months per year it will point towards the Galactic plane and away from its primary science fields. As stated in Laureijs et al. (2011), it is intended that some of this time will be devoted to other legacy science. A planetary microlensing survey is one option described in Laureijs et al. (2011) and is being actively evaluated by the Euclid Exoplanets Working Group.

The similarity of hardware requirements for dark energy and exoplanet microlensing space missions has been recognized for some time (Bennett & Rhie 2002), and most recently by the 2010 US Astrophysics Decadal Review (Blandford et al. 2010). This review recommended the merger of three mission concepts into one mission, the *WFIRST* (Green et al. 2012). Two of the core science objectives for *WFIRST* are a dark energy survey and an exoplanets survey using microlensing. In the baseline *WFIRST* concept, the microlensing survey will total 432 d, somewhat longer than will be feasible for ExELS.

4 THE MANCHESTER-BESANÇON MICROLENSING SIMULATOR (MAB μ LS)

We have designed the MAB μ LS – pronounced *may-buls* – to perform detailed simulations of the ExELS concept. MAB μ LS is the first microlensing simulator to use a combination of a population synthesis Galactic model with a realistic treatment of imaging photometry. This means that every aspect of the simulation, including the event rate calculations, blending and photometry are simulated self-consistently.

Several key ingredients are needed in order to simulate any microlensing survey. A simulator must draw its simulated events from a Galactic model and distributions of the event parameters. It must simulate the observations of the survey, and finally, it must also simulate the detection criteria used to select its sample of events. It is also necessary to make a choice as to the complexity of the microlensing model used to simulate events. For example, is the lens composed of a single mass or multiple components? Are higher order effects such as parallax and orbital motion included? In the rest of this section, we will discuss both how MAB μ LS implements each component of the simulation and the choice of parameters we use in the simulation of ExELS. Unless stated otherwise, we have taken the survey parameters from the *Euclid* Red Book (Laureijs et al. 2011).

4.1 The Besançon Galactic model

Underpinning the MAB μ LS microlensing event generation is the Besançon model (Robin & Creze 1986; Robin et al. 2003, 2012), a population synthesis model of the Galaxy. The Besançon model comprises five main stellar populations, a spheroid (stellar halo), thin and thick discs, a bar and bulge. The stars of each population are assumed to be formed from gas for input models of star formation history and initial mass function (IMF). The stars are aged according to model evolutionary tracks to their present-day state (Haywood, Robin & Creze 1997). This determines the distribution of stellar bolometric fluxes, which are converted to colours and magnitudes using stellar atmosphere models convolved with standard bandpass templates in various photometric systems.

The spatio-kinematic distribution of the disc stars is determined by integration of a self-consistent gravitational model using the Poisson and Boltzmann equations. Finally, the observed colours and magnitudes are corrected for extinction using a three-dimensional dust model (Marshall et al. 2006). A limited number of model parameters are then optimized to reproduce observed star counts and kinematics. The output of the model is an artificial catalogue of stellar photometry and kinematics for a survey of specified sensitivity and areal coverage.

The Besançon model is in constant development (e.g. Robin et al. 2012). In this work, we use version 1106 of the Besançon model, though an updated version of the model has been released since. In subsequent models, the properties of the Galactic bar and bulge (see below) change somewhat from those we use here. Below, we briefly overview the properties of the main stellar components used to generate microlensing events in MAB μ LS. The solar Galactocentric distance in the model is 8 kpc.

4.1.1 The stellar halo

The stellar halo is modelled as being formed by a single burst of star formation at 14 Gyr, with metallicity centred at $[\text{Fe}/\text{H}] = -1.78$ and with a dispersion of 0.5. It has a triaxial velocity distribution with dispersions $(\sigma_U, \sigma_V, \sigma_W) = (131, 106, 85) \text{ km s}^{-1}$. Its density is small everywhere, even at the Galactic Centre, and so it contributes only marginally to the optical depth and microlensing event rate.

4.1.2 The bar

The bar, altered from the bulge-like component used by Kerins et al. (2009), consists of a boxy triaxial distribution, similar to that described by Picaud & Robin (2004), but with a Gaussian density law as opposed to a Freudreich (1998) sech^2 law (Robin et al. 2012). The major axis of the triaxial structure lies at an angle of 12.5° relative to the Sun–Galactic Centre line of sight and has scalelengths $(X, Y, Z) = (1.63, 0.51, 0.39) \text{ kpc}$, where the x direction is parallel to the major axis and the x and y axes lie in the Galactic plane. It is truncated at a Galactocentric radius of 2.67 kpc. The bar rotates as a solid body with a speed of $40 \text{ km s}^{-1} \text{ kpc}^{-1}$. The velocity dispersions in the bar along the axes defined above are $(113, 115, 100) \text{ km s}^{-1}$. The central stellar mass density of the bar, excluding the central black hole and clusters, is $19.6 \times 10^9 \text{ M}_\odot \text{ kpc}^{-3}$.

Embedded within the bar is also an additional component (somewhat different from the ‘thick bulge’ component in Robin et al. 2012). However, in the version of the model we use here, its density is smaller by $\sim 10^{-4}$ times that of the bar, so we do not describe it further. We use the terms ‘bar’ and ‘bulge’ interchangeably from here onwards to mean the bar component of the Besançon model.

The stellar population of the bar is assumed to form in a single burst 7.9 Gyr ago (Picaud & Robin 2004), following Girardi et al. (2002). The bar IMF (dN/dM) scales as M^{-1} between 0.15 and 0.7 M_\odot , and follows a Salpeter slope above this mass. The population has a mean metallicity $[\text{Fe}/\text{H}] = 0.0$ with dispersion 0.2 and no metallicity gradient. The stellar luminosities are calculated using Padova isochrones (Girardi et al. 2002).

4.1.3 The thick disc

The thick disc is modelled by a single burst of star formation at 11 Gyr. Its properties have been constrained using star counts by Reylé & Robin (2001). The thick disc contributes only marginally to the microlensing event rate, so we do not describe it in detail. Its parameters are described by Robin et al. (2003).

4.1.4 The thin disc

The thin disc is assumed to have an age of 10 Gyr, over which star formation occurs at a constant rate. Stars are formed with a two-slope IMF that scales as a power law $M^{-1.6}$ from 0.079 to 1 M_\odot and M^{-3} above, based on the *Hipparcos* luminosity function (e.g. Haywood et al. 1997), with updates described by Robin et al. (2003). Stars below 1 M_\odot follow the evolutionary tracks of Vandenberg, Bergbusch & Dowler (2006), while those above follow Schaller et al. (1992) tracks. The thin disc follows an Einasto (1979) density profile with a central hole. The density normalization, kinematics and metallicity distribution of the disc depend on stellar age, with seven age ranges defined, whose parameters are given by Robin et al. (2003). The Solar velocity is $(U_\odot, V_\odot, W_\odot) = (10.3, 6.3, 5.9) \text{ km s}^{-1}$, with respect to the local standard of rest $V_{\text{LSR}} = 226 \text{ km s}^{-1}$. The disc has a scalelength of 2.36 kpc, and the hole has a scalelength of 1.31 kpc, except for the youngest disc component which has disc and hole scalelengths of 5 and 3 kpc, respectively. The disc is truncated at 14.0 kpc. The scaleheight of the disc is computed self-consistently using the Galactic potential via the Boltzmann equation as described by Bienayme, Robin & Creze (1987). Also modelled in the disc are its warp and flare (Reylé et al. 2009).

4.1.5 Extinction

Extinction is computed using a three-dimensional dust distribution model of the inner Galaxy ($|\ell| < 100^\circ$, $|b| < 10^\circ$), built by Marshall et al. (2006) from analysis of 2MASS data (Cutri et al. 2003) using the Besançon model. Marshall et al. (2006) did this by comparing observed, reddened stars to unreddened simulated stars drawn from the Besançon model. From this, the extinction as a function of distance along a given line of sight is computed by minimizing χ^2 between observed and simulated $J - K_s$ colour distributions. The resulting map has an ~ 15 arcmin resolution in ℓ and b , and a distance resolution of $\sim 0.1\text{--}0.5 \text{ kpc}$, resulting from a compromise between angular and distance resolution.

4.1.6 Other components

The Besançon model also takes account of other Galactic components, including the mass due to the dark matter halo and interstellar medium. The details of these components are given by Robin et al. (2003). White dwarfs are included in the model separately to normal stars, with separate densities and luminosity functions determined from observational constraints (Robin et al. 2003, and references therein). The evolutionary tracks and atmosphere models of Bergeron, Wesemael & Beauchamp (1995) and Chabrier (1999) are used to compute their colours and magnitudes.

4.2 Microlensing with the Besançon model

Following the method of Kerins et al. (2009), MAB μ LS uses two star lists output by the Besançon simulation to construct catalogues of possible microlensing events and calculate their properties. The first list, the source list, is drawn from the Besançon model using a single magnitude cut in the primary observing band of the survey. A second list, the lens list, is drawn from the model without a magnitude cut. Both source and lens lists are truncated at a distance of 15 kpc to improve the statistics of nearer lenses and sources that are much more likely to be lensed/lensing.

Table 1. The magnitude range and the average number of stars $\langle N_* \rangle$ in the Besançon model star catalogues used in this work. Bright, moderate and faint are the three levels of catalogues used to build the simulated images.

Catalogue	Magnitude range	Solid angle (deg ²)	$\langle N_* \rangle$
Source	$10 < H_{\text{vega}} \leq 24$	2×10^{-4}	232 19
Lens	$-\infty < H_{\text{vega}} \leq \infty$	2×10^{-4}	329 33
Bright	$-\infty < H_{\text{vega}} \leq 15$	1×10^{-3}	441
Moderate	$15 < H_{\text{vega}} \leq 24$	2×10^{-5}	2312
Faint	$24 < H_{\text{vega}} \leq \infty$	2×10^{-5}	967

Overall microlensing event rates are calculated along multiple lines of sight, with spacing set by the resolution of the Marshall et al. (2006) dust map. The total rate due to each pair of source and lens lists, about the line of sight (ℓ, b) , is

$$\Gamma(\ell, b) = \frac{\Omega_{\text{los}}}{\delta\Omega_s} \sum_{\text{Sources}} \left(\frac{1}{\delta\Omega_l} \sum_{D_l < D_s} 2\theta_E \mu_{\text{rel}} \right), \quad (2)$$

where Ω_{los} is the solid angle covered by a dust-map resolution-element, and $\delta\Omega_s$ and $\delta\Omega_l$ are the solid angles over which the source and lens catalogues are selected, respectively. The rate is calculated over all possible source–lens pairs to minimize the noise of counting statistics. The average sizes of all the catalogues used in this work are listed in Table 1.

To simulate microlensing, MABμLS draws sources and lenses from their respective lists with replacement, requiring the source to be more distant than the lens. From the source and lens parameters, the Einstein radius and time-scale are computed, as well as the rate weighting assigned to the event

$$\gamma = u_{0\text{max}} \theta_E \mu_{\text{rel}}, \quad (3)$$

where $u_{0\text{max}}$ is the maximum impact parameter of the event; how $u_{0\text{max}}$ is determined is discussed in the following sections. Events are simulated and those that pass the detection criteria are flagged. The rate of detections in a given dust-map element is the sum of the weights of detected events normalized to the sum of the rate weightings for all the simulated events – this is essentially a detection efficiency. The detection efficiency is then multiplied by the total line-of-sight rate computed in equation (2) to yield the expected detection rate for $0.25 \times 0.25 \text{ deg}^2$, the size of the dust-map element. These rates are then summed over all the dust-map elements to yield the total simulation event rate.

For the ExELS simulations, we restrict the source magnitude to a vega-based H -band magnitude $H_{\text{vega}} < 24$. This corresponds to an AB magnitude limit of $H_{\text{AB}} < 25.37$. Unless otherwise noted, AB magnitudes will be used throughout the paper.

4.2.1 Normalization of the event rate

The absolute number of stars in the Besançon model has been set by normalizing their number density to match star counts along a number of lines of sight that sample the different components of the Galaxy (Robin et al. 2003). This process will only be accurate down to the limiting magnitude of the star count data, and it is possible that the number of fainter stars predicted by the model could be incorrect. While these fainter stars may not contribute to star counts, they do contribute to the microlensing event rate, either as lenses or sources. It is therefore important to make sure that the microlensing event rates predicted by the Besançon model match those that are observed.

The microlensing event rate is a potentially powerful but complex probe of Galactic structure because it depends on the kinematics of the lens and source populations as well as the lens mass function. Often, surveys aim instead to measure the microlensing optical depth, which is much more cleanly defined as it only depends only on the distribution of lenses and sources along the line of sight. The total event rate Γ is related to the optical depth τ by (e.g. Paczyński 1996)

$$\Gamma \propto \frac{N_* \tau}{\langle t_E \rangle}, \quad (4)$$

where N_* is the number of monitored sources and $\langle t_E \rangle$ is the average event time-scale. We can verify the microlensing event rate predicted by the Besançon model by comparing each of the quantities on the right-hand side of equation (4) to measured values, and make a correction to the rate if required.

In the bulge region, the Besançon model has been normalized to star counts from the 2MASS survey (Cutri et al. 2003; Robin et al. 2012), which is relatively shallow compared to the sources that *Euclid* will observe. The number counts of fainter sources are extrapolated using the IMF and extinction maps, and any uncertainties in these will propagate to the source counts. There is a relative paucity of deep star count measurements in the bulge with which to test the Besançon model assumptions, with published measurements only along a single line of sight close to our proposed *Euclid* fields. To assess the validity of N_* , we compare this measurement of the luminosity function in Baade’s window (Holtzman et al. 1998) to the Besançon star catalogue produced for the same line of sight. Fig. 1 shows both luminosity functions. There is good agreement between the two luminosity functions in the magnitude range $17 < I_{\text{vega}} < 20$, but fainter than this the Besançon model underpredicts the number of stars. Integrated over the whole range of the Holtzman et al. (1998) luminosity function, the Besançon model predicts 32.46×10^6 stars per square degree, but Holtzman et al. (1998)

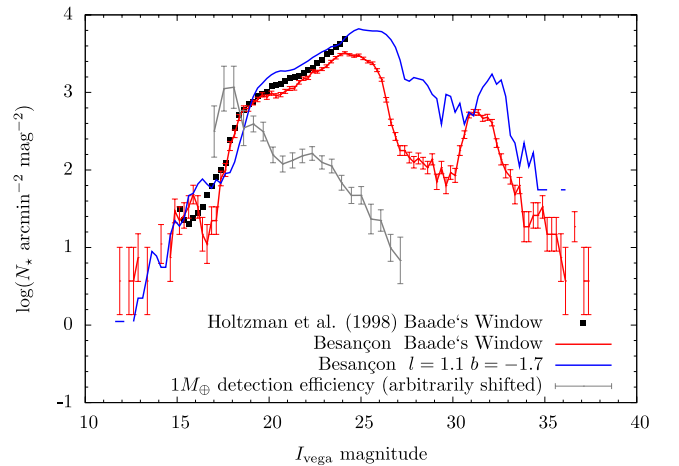


Figure 1. Comparison of the luminosity function in the bulge as measured by Holtzman et al. (1998) in Baade’s window ($\ell = 1, b = -3.9$) to that of the Besançon model at the same location. The measured luminosity function, shown by the black line, has been returned to the I -band apparent magnitude scale by adopting the distance modulus ($\mu = 14.52$) and extinction ($A_I = 0.76$) values of Holtzman et al. (1998). The red line shows the Besançon model luminosity function at Baade’s window, while the blue line shows the Besançon model luminosity function at the centre of the ExELS fields ($\ell = 1.1, b = -1.7$). The grey line shows the Earth-mass planet detection efficiency for *Euclid* as a function of source I_{vega} magnitude (arbitrarily shifted on the log scale).

measure 42.06×10^6 stars per square degree. To correct the event rate for this lack of stars requires multiplying by a factor of 1.30. While we adopt this correction, we caution that a significant fraction of the discrepancy arises from the faintest part of the luminosity function, where Holtzman et al. (1998) argue that their completeness corrections are uncertain. Beyond the faintest bin of the Holtzman et al. (1998) luminosity function, we might worry that the number of stars keeps on increasing in reality, while in the Besançon model it begins to fall off, suggesting that a larger correction factor would be required. However, average extinction in the ExELS fields ($A_I = 1.73$ at a distance of 8 kpc; Marshall et al. 2006) is nearly 1 mag more than $A_I = 0.76$, the value adopted by Holtzman et al. (1998) in their Baade’s window field. This implies that in the ExELS fields the Holtzman et al. (1998) luminosity function extends down to $I_{\text{vega}} \approx 25.2$. At this source magnitude, the planet detection efficiency for *Euclid* has fallen to roughly a third of the average at brighter magnitudes, and falls rapidly as the sources get fainter. Therefore, while there may be more faint stars that the Besançon model is missing, including these source stars will not significantly increase the number of planet detections.

The optical depth in the Galactic bulge has been measured to two different source populations: red clump giants and difference imaging analysis (DIA) sources. Measurements of DIA optical depths are typically slightly higher than those for clump giant sources. Clump giants are abundant, bright standard candles, and those in the bulge can be easily recognized and isolated by their position on a colour–magnitude diagram. They therefore make an ideal tracer population of the bulge. DIA sources, however, are less clearly defined, as they depend on the sensitivity of the survey. Due to this difficulty of defining the DIA source population, we only compare the Besançon model to measured red clump optical depths, which have been measured by the Massive Compact Halo Objects (MACHO; Popowski et al. 2005), Experience de Recherche d’Objects Sombres (Eros; Hamadache et al. 2005) and OGLE (Sumi et al. 2006) surveys. Fig. 2 shows the red clump optical depth measurements of each of these surveys as a function of absolute Galactic

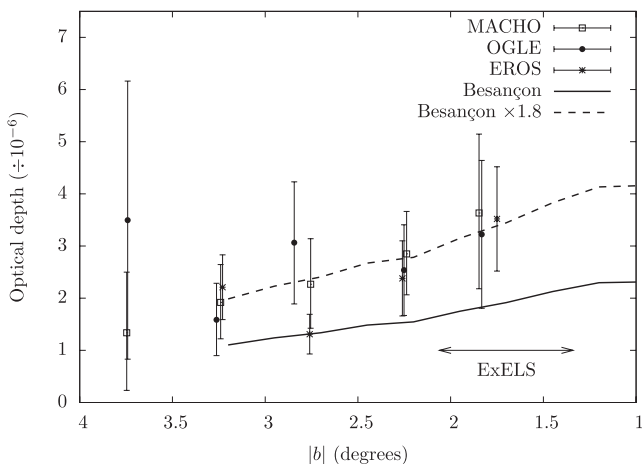


Figure 2. A comparison of measured optical depths to red clump giants to those calculated from the Besançon model. The open square, filled circle and asterisk data points show results from the MACHO (Popowski et al. 2005), OGLE (Sumi et al. 2006) and EROS (Hamadache et al. 2006) surveys, respectively. The solid line shows the average optical depth to red clump stars selected from the Besançon model based on their absolute magnitudes and colours. The dashed line shows the same line as the solid curve, but multiplied by a constant 1.8 to match the data.

latitude, together with the average optical depth to red clump stars as predicted by the Besançon model. The Besançon optical depths are averaged over the longitude range $-0.525 < \ell < 2.725$. It is clear that the Besançon optical depth is somewhat lower than the measured optical depth. Multiplying the Besançon model optical depths by a constant factor of 1.8 brings the predictions into good agreement with the measurements.

The average time-scale reported by microlensing experiments is somewhat ill defined due to the arbitrary time-scale cutoffs applied to their event samples, but are typically in the range of 20–30 d. The average time-scale calculated from the time-scale distribution presented in Fig. 13 is 21.4 d without applying any detection criteria and 29.2 d for events detected above baseline. The average time-scale of the Sumi et al. (2011) sample is 26.0 d. The sample detected above baseline is most comparable to the Sumi et al. (2011) sample, but is not directly comparable. As the difference is of the order of 10–20 per cent and the samples are not directly comparable, we choose not to make a correction to the event rate based on the time-scales.

Combining the required correction factors for optical depth and source counts, we conclude that the microlensing event rates predicted by the Besançon model likely require a correction factor

$$f_{1106} = 1.8 \times 1.30 = 2.33, \quad (5)$$

where the subscript emphasizes the fact that this scaling is only applicable to the version of the Besançon model we are using. We have multiplied all raw results by this factor throughout the paper. To account for further uncertainty in the overall event rate, we define an additional multiplicative factor f_{Γ} , with which all the event rates and numbers of planet detections should be multiplied. In this paper, we advocate for a value $f_{\Gamma} = 1$. Note, however, that Green et al. (2012) choose a value $f_{\Gamma} = 1.475$ to compromise between different values of the planet detection efficiency determined from MABμLS and simulations following Bennett & Rhie (2002).

One possible cause of the low predicted optical depth could be missing low-mass stars and sub-stellar objects too faint to be included in star counts. The lower cutoff of the bulge mass function in the Besançon model is $0.15 M_{\odot}$. Extending the mass function down to $\sim 0.03 M_{\odot}$, keeping the same low-mass slope (M^{-1}), would account for the missing optical depth (see Calchi Novati et al. 2008 for a discussion of the effect of the mass function of microlensing event rates). Adding such low-mass stars to the star catalogues would increase the number of planet detections by a factor larger than the increase in optical depth, because the mass ratio of planets around these stars would be larger than the mass ratio of planets around a star of the average stellar mass in the catalogues. Another possible cause of the low optical depth is the lack of high-mass stellar remnants – neutron stars and black holes, which are not included in the Besançon catalogues. Should these be the cause of the low optical depth, the number of planet detections would not increase as much as the optical depth, because even if planets remained around these objects, their mass ratios would be smaller than the average in the unmodified catalogues. Other possible causes of the optical depth discrepancy, such as problems with Galactic structure, would cause the number of planet detections to change in the same way as the microlensing event rate. Note that in all the scenarios discussed here, the average time-scale is affected – adding low-mass stars decreases the average time-scale, giving a further boost to the event rate, while adding high-mass remnants increases the average time-scale, further suppressing any boost. Comparing the Besançon time-scale distribution to that observed by Sumi et al. (2011) (see Fig. 13) suggests that the Besançon model is missing short

time-scale events, but each time-scale distribution has different selection criteria, so it is impossible to draw firm conclusions.

4.3 The microlensing events

MAB μ LS uses user-supplied functions to compute microlensing light curves including any effects that the user wants to model. For this work, we modelled only planetary lens systems composed of a single planet orbiting a single host star. As we want to investigate the planet detection capability of ExELS as a function of planet mass M_p and semimajor axis a , we chose to simulate systems with various fixed values of planetary mass in the range $0.03\text{--}10^4 M_\oplus$ and semimajor axis distributed logarithmically in the range $0.03 < a < 30$ au. We assume a circular planetary orbit that is inclined randomly to the line of sight. The orbital phase at the time of the event is again random; we do not model the effects of orbital motion in the lens. The impact parameter and angle of the source trajectory are distributed randomly, with the impact parameter in the range $u_0 = 0\text{--}u_{0\text{max}}$. For ExELS simulations, we choose $u_{0\text{max}} = 3$. While it may be the case that some of the stellar microlensing events with $u_0 \approx 3$ will not be detected, it is still possible for planets to cause detectable signals.

The planetary microlensing light curves are computed assuming that the source has a uniform intensity profile (in other words, no limb darkening). Test simulations including the effect of limb darkening (which is small in the infrared) showed that inclusion of the effect would change the number of Earth-mass planet detections by less than 1 per cent. The finite-source magnification is computed using the hexadecapole approximation when finite-source effects are small (Gould 2008; Pejcha & Heyrovský 2009) and the contouring method when they are not (Gould & Gauchere 1997; Dominik 1998). Finite-source effects are accounted for in single-lens light curve calculations using the method of Witt & Mao (1994). When fitting light curves with the single-lens model, we use a finite-source single-lens model if the impact parameter $u_0 < 10\rho$, where ρ is the ratio of angular source radius to the angular Einstein radius. Otherwise the point-source single-lens model is used.

4.3.1 Free-floating planets

Observations from nearby star clusters, as well as tentative evidence from ground-based microlensing surveys, suggests that planets can occur unbound from any host, sometimes referred to as free-floating planets. If free-floating planets exist in significant numbers then ExELS should detect them as relatively brief single-lens microlensing events.

At this stage, we have no clear information to allow us to characterize a Galactic population of free-floating planets with confidence. What we know from young star clusters like Sigma Orionis is that brown dwarfs ($0.072\text{--}0.013 M_\odot$) and massive free-floating planets ($0.013\text{--}0.004 M_\odot$) are as numerous as low-mass stars with masses in the interval $0.25\text{--}0.072 M_\odot$ (Peña Ramírez et al. 2012). However, given the uncertainties over the characteristics of a Galactic-wide distribution of planets, we adopt a simple scalable assumption of one free-floating planet of mass M_{ffp} per Galactic star.

As free-floating planets are single, point-mass lenses we treat them in a separate MAB μ LS simulation. Each lens star drawn from the Besançon simulation is replaced by a planet of mass M_{ffp} . We simulate a range of values for M_{ffp} from 0.03 to $10^4 M_\oplus$. We assume that the planets retain the same kinematics, but the fundamental microlensing properties such as the Einstein radius change to reflect the reduced mass. Ejected planets may well have a somewhat

larger velocity dispersion than their original hosts, in which case the rate of free-floating planet events increases proportionately and the time-scale decreases inversely with their velocity. We assume that free-floating planets emit no detectable light, which is a good assumption for typical distances at which planets are detectable through microlensing. Each light curve is calculated using the finite-source single-lens model. The impact parameter is chosen to lie in the range $u_0 = 0\text{--}u_{0\text{max}}$, where we choose $u_{0\text{max}} = 1$ to remain conservative, and we require that the time of peak magnification lies within an observing season (unlike for the standard simulations).

4.4 Euclid observing strategy

The ExELS survey must be capable of detecting planets at least down to Earth masses, which means that we require an observing cadence of no more than 20 min between repeat observations of the same field. It must also monitor enough source stars over a sufficiently long observing baseline to ensure a healthy detection rate. As shown by Kerins et al. (2009), the event rate is optimized at near-infrared wavelengths, suggesting that the NISP camera should be the primary instrument for ExELS. In Section 6.1, we show that this is indeed the case, despite the significantly worse resolution of the NISP instrument relevant to the optical VIS instrument.

In order to achieve a cadence of no worse than 20 min, ExELS will be able to monitor up to three target fields of $\sim 0.5 \text{ deg}^2$ with a total exposure of 270 s per pointing, split into stacks of three (*Y*- and *J*-band) or five (*H*-band) exposures with NISP. We assume that there is 5 s of dead time between the exposures of a stack. The VIS instrument pointings consist of a single 540 s exposure. We assume a baseline slew and settle time of 85 s, though in Section 6.3, we also consider the effect of a substantially longer slew and settle time. We assume that any readout, filter wheel rotation and data downlink is performed during slewing. Some of these parameters are summarized in Table 2.

We simulate a total observing baseline of 300 d for ExELS, spread over 5 years with two 30 d seasons per year. This strategy is determined by the design of the spacecraft's sun shield. This restricts *Euclid* to observing fields with solar aspect angles between 89° and 120° . As the Galactic bulge lies near to the ecliptic, *Euclid* can only observe bulge fields uninterrupted for up to 30 d, twice per year. It should be stressed that a 10-month survey represents a firm theoretical maximum that could be possibly achieved over 5 years. In practice, the cosmology primary science will likely prohibit much legacy science being undertaken in the first few years of the mission, so that a six-month exoplanet survey likely represents a more achievable goal during the 6-year primary cosmology mission. It is possible that, if *Euclid* remains in good health beyond 6 years, a full 10-month programme could be completed after the cosmology programme is complete. We therefore investigate the exoplanet science returns possible for a survey of up to 10 months total time. We assess the impact of shorter total baselines in Section 5.

For the ExELS simulation, we use three contiguous *Euclid* pointings aligned parallel to the Milky Way plane, with the central field located at Galactic coordinates $l = 1:1$ and $b = -1:7$ (J2000), as shown in Fig. 3. Each *Euclid* field covers $0.76 \times 0.72 \text{ deg}^2$ on the sky, giving a total ExELS survey area of 1.64 deg^2 . We conservatively assume that most of the observations are taken with NISP in only one filter (we show in Section 6 that *H* band is the best filter choice), at a cadence of roughly one observation every 20 min. Conservatively, we add colour information from the two other NISP filters and the VIS camera at a rate of only one observation every 12 h. This conservative assumption guarantees that we will not be

Table 2. Parameters of the *Euclid* telescope and detectors. Unless footnoted, all parameter values have been drawn from the Laureijs et al. (2011). Values in brackets are values adopted for a longer slew time of 285 s rather than our baseline assumption of 85 s. Where necessary parameters are explained further in the text.

Telescope parameters				
Diameter (m)	1.2			
Central blockage (m)	0.4			
Slew + settle time (s)	85(285)			
Detector parameters				
Instrument	VIS	NISP		
Filter	<i>RIZ</i>	<i>Y</i>	<i>J</i>	<i>H</i>
Size (pixels)	24 k × 24 k	8 k × 8 k		
Pixel scale (arcsec)	0.1	0.3		
PSF FWHM (arcsec)	0.18	0.3 ^a	0.36 ^a	0.45 ^a
Bias level (e [−])	380 ^b	380 ^b		
Full well depth (e [−])	2 ¹⁶	2 ¹⁶		
Zero-point (ABmag)	25.58 ^c	24.25 ^d	24.29 ^d	24.92 ^d
Readout noise (e [−])	4.5	7.5 ^a	7.5 ^a	9.1 ^a
Thermal background (e [−] s ^{−1})	0	0.26	0.02	0.02
Dark current (e [−] s ^{−1})	0.00056 ^e	0.1 ^a		
Systematic error	0.001 ^b	0.001 ^b		
Diffuse background (ABmag arcsec ^{−2})	21.5 ^f	21.3 ^f	21.3 ^f	21.4 ^f
Exposure time (s)	540(270)	90	90	54
Images per stack	1	3(1)	3(1)	5(2)
Readout time (s)	<85	5 ^b		

^aSchweitzer et al. (2010). The readout noise depends on the number of non-destructive reads; see the text for further details.

^bAssumed in this work.

^cCropper, private communication.

^dSeidel, private communication.

^eCCD203-82 data sheet, issue 2, 2007. e2v technologies, Elmsford, NY, USA.

^fCalculated based on field locations, taking values for the zodiacal background from Leinert et al. (1998), and assuming an extra 0.2 mag from other sources such as scattered light.

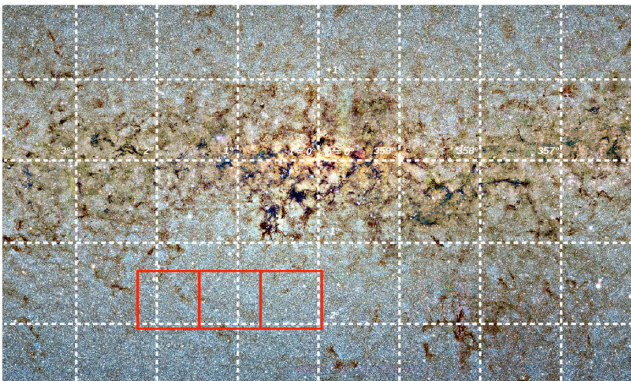


Figure 3. The approximate location of the three ExELS field pointings (solid line rectangles) assumed for the simulation, with the middle of the three fields centred at $l = 1^\circ 1$, $b = -1^\circ 7$. Each ExELS field has dimensions of $0.76 \times 0.72 \text{ deg}^2$. The background image of the Galactic Centre is a near-infrared mosaic of images from the Vista Variables in the Via Lactea Survey (VVV Survey; Saito et al. 2012). Background image credit: Mike Read (Wide-field Astronomy Unit, Edinburgh) and the VVV team.

limited by telemetry rate restrictions. However, in Section 6.1, we consider the benefits of simultaneous NISP and VIS imaging. For the hot exoplanet science investigated in Paper II, we note that it is important to achieve high-cadence observations with both VIS and NISP instruments. Therefore, strong limitations in telemetry could impact somewhat upon the hot exoplanet science, but is unlikely to impact significantly upon the cold exoplanet science discussed here.

The number of planets which can be detected by ExELS will be governed by the overall rate of microlensing within the survey area, though only a small fraction of these will have detectable planetary signatures. The expected overall number of microlensing events (with or without planet signatures) that would be detected as significantly magnified by ExELS is $\sim 27\,000$ events with $u_0 \leq 3$ over the course of a 300-d survey. This is in excess of the total number of microlensing events discovered by all ground-based microlensing surveys since they started operations 20 years ago. However, some of these events may not be well characterized if they peak outside of one of the observing seasons. Placing the restriction that the time of peak magnification, t_0 , must be contained within one of the observing seasons lowers the overall number to ~ 9800 events (~ 5700 events with $u_0 < 1$) for a 300-d campaign, or about 1000 events per month. This is an improvement of a factor of ~ 65 in detection rate per unit time per unit area over the OGLE-IV survey (Udalski 2011) in its best field, which yields ~ 15 events per month per deg^2 . Between now and *Euclid*'s scheduled launch in 2019, the OGLE-IV survey observing the bulge ~ 8 months per year can detect a similar number of microlensing events to *Euclid* observing for 10 months total. However, the ExELS survey will be much more sensitive to low-mass planets per event.

4.5 Photometry

In order to accurately account for the effects of severe stellar crowding on photometry of Galactic bulge stars, MAB μ LS produces simulated images for each microlensing event it simulates. The source and lens stars of each microlensing event are injected into the image, with the source star's brightness updated at each epoch. Finally, relative aperture photometry is performed to measure the source brightness in each image.

The image is constructed from a smooth background component and stars drawn from the Besançon model catalogues. Stars are added to the images at random locations on a fine (9×9) sub-pixel grid, using numerical PSFs that have been integrated over pixels. Each star is tracked so that it is included at the correct position and brightness in images taken with different filters or instruments. In this way, blending is computed consistently throughout the simulation. In order to avoid small-number statistics for bright stars without using huge catalogues, we use tiered catalogues with different magnitude ranges, as listed in Table 1.

At each epoch a new realization of the counts is made. Counts from stars, smooth backgrounds and instrumental backgrounds (thermal background and dark current) are Poisson realized, and fluctuations from readout noise are Gaussian realized. Photometry is performed on both the realization and a 'true' image in a small, square, 3×3 pixel aperture² around the microlensing source with the true (input) value of the smooth background subtracted, i.e. the

² Testing showed that the 3×3 aperture was the optimum aperture size for simple aperture photometry in our crowded fields.

number of counts from stellar sources in the aperture is measured to be

$$N = \sum_i^{N_{\text{pix}}} (N_{\text{tot},i} - \langle N_{\text{bg}} \rangle), \quad (6)$$

where $N_{\text{tot},i}$ is the total number of counts in pixel i and $\langle N_{\text{bg}} \rangle$ is the expectation of the counts in each pixel due to all the sources of smooth background, astrophysical and instrumental. An additional Gaussian fluctuation of variance $(\sigma_{\text{sys}}N)^2$ is added to the final realization of the photometric measurement to simulate the effect of a systematic error floor. The photometric error is calculated as

$$\sigma_N^2 = \sum_i^{N_{\text{pix}}} (N_{\text{tot},i} + \sigma_{\text{read}}^2) + N^2 \sigma_{\text{sys}}^2, \quad (7)$$

where $N_{\text{pix}} = 9$ is the number of pixels in the aperture. The χ^2 of the realized photometry relative to the ‘true’ photometry is the χ^2 of the true model which is used to calculate the $\Delta\chi^2$ detection statistic (see the next section). Should the number of counts in a pixel (including an assumed bias level) exceed the full well depth of the detector, then the pixel saturates. If that pixel lies in the photometry aperture, the data point is removed from further calculations.

It can be argued that the aperture photometry we simulate here is not appropriate for crowded fields, and that some form of PSF fitting photometry would be more realistic. While it is the case that the photometry that is performed on *Euclid* data will utilize the well-known properties of the PSF to increase the photometric accuracy, it should be noted that over the small number of pixels where we perform photometry, a boxcar is a reasonable approximation of the undersampled PSF. To check that the photometric method we use does not significantly impact the number of planet detections, we ran a test simulation performing photometry over a larger aperture,³ weighting the number of counts in each pixel by the intensity of the PSF in that pixel – this weighting approximates the performance of PSF fitting photometry. For an *H*-band survey and Earth-mass planets, we find that weighted photometry increases the number of planet detections by 6 ± 2 per cent. The improvement will be larger for less massive planets and smaller for more massive planets, but in all cases will be too small to significantly affect our results. The improvement will be smaller for all other bands, because the smaller PSF in each case, and the smaller pixels on the VIS instrument, reduces the effect of blending. Indeed, the small under prediction of planet yields will likely be compensated by effects that we do not model in our simulations (e.g. cosmic rays or common problems that affect infrared arrays such as ghosting, charge diffusion or non-uniform pixel response functions), which are far more likely to degrade photometry than improve it.

The properties of the detector/filter combinations that we model are listed in Table 2. We note the following about the parameters listed in the table:

(i) The zero-point is the AB magnitude of a point source, which would cause one count per second in the detector, after all telescope and instrument inefficiencies have been accounted for. The *Euclid* zero-points assume end-of-life instrument performance (Cropper, private communication; Seidel, private communication).

(ii) We distinguish between dark current and thermal background. The dark current is the rate of counts induced by thermal

sources *within the detector pixels*, and is independent of the observing band. The thermal background is the count rate due to thermal photons emitted by all components of the spacecraft that hit the detector, and is therefore affected by the choice of filter.

(iii) For the *Euclid* simulations, we assume that the smooth background is due primarily to zodiacal light. To account for any additional smooth backgrounds we add an additional component with 20 per cent of the intensity of the zodiacal light. The zodiacal light background is calculated for each band at an elongation of 90° in the ecliptic using data given by Leinert et al. (1998).

(iv) The VIS *RIZ* and NISP *Y* bands are not included in the Besançon model, so we assume that the AB magnitude of a star in the *RIZ* band is the average of its *R* and *I* AB magnitudes, and similarly we assume that the *Y*-band magnitude is the average of *I* and *J*.

Should a pixel within the photometry aperture saturate, the data point is flagged and is not included in the subsequent analysis. We do not include the effects of cosmic rays in the images, except implicitly through the use of end-of-life instrument sensitivity values. For the *Euclid* simulations, cosmic rays will only significantly affect observations with the VIS instrument, because the NISP instrument, made up of infrared arrays, will use up-the-ramp fitting with non-destructive reads (Fixsen et al. 2000) to reduce read-out noise and correct detector non-linearities (Beletic et al. 2008; Schweitzer et al. 2010). As a consequence of the multiple reads, up-the-ramp fitting mitigates against data loss due to cosmic rays and saturation. In order to ensure conservatism, we assume data with saturated pixels is lost completely. Currently, we simulate the NISP instrument as a conventional CCD, but with variable read-noise determined by a fundamental read-noise (13 e^-) and the number of non-destructive reads during an exposure, which we assume occur at a constant rate of once every $\sim 5 \text{ s}$ (Schweitzer et al. 2010). We do not currently simulate the more complicated effects of charge smearing (see, e.g., Cropper et al. 2010) and ghosts from bright stars.

For the *Euclid* simulations, we use numerical PSFs computed for each instrument and each band. The NISP PSFs are computed near the edge of the detector field of view and include the effect of jitter and instrument optics in the worst case scenario (Seidel, private communication). The VIS PSF is similarly computed (Cropper, private communication). Fig. 4 shows an example of a simulated, colour-composite image of a field with a microlensing event at its centre. The very brightest, reddest stars in the image are bright bulge giants of $\sim 1 M_\odot$ and $\sim 80\text{--}120 R_\odot$. The much more numerous, but still bright and red, stars are red clump giants in the bulge; bluer stars of a similar brightness are main-sequence F-stars in the disc. The fainter, resolved stars are turn-off and upper-main-sequence stars in the bulge. The figure also shows an approximate representation of the scale of the NISP instrument, which is constructed from 4×4 HgCdTe infrared arrays, each of 2048×2048 pixels covering $10 \text{ arcmin} \times 10 \text{ arcmin}$, for a total detector area of 0.47 deg^2 ; the gaps between detectors are approximately to scale. We do not include these gaps in the simulation and assume the instrument is a single 8192×8192 -pixel detector. The lower section of Fig. 4 shows a set of zoomed-in image sections, centred on the microlensing event at peak and at baseline, in each of the NISP and VIS bands. Note the diffraction spikes and Airy rings in the VIS images; such spikes and rings can significantly affect photometry of faint sources. Fig. 5 shows the light curve of the simulated event with peak magnification $\mu = 28$ that occurs in the example image, including the points that are lost to saturation. For the sake of computational

³ The radius of the aperture was 0.92 arcsec, covering 29 pixels. This was chosen by experimentation to optimize the photometry.

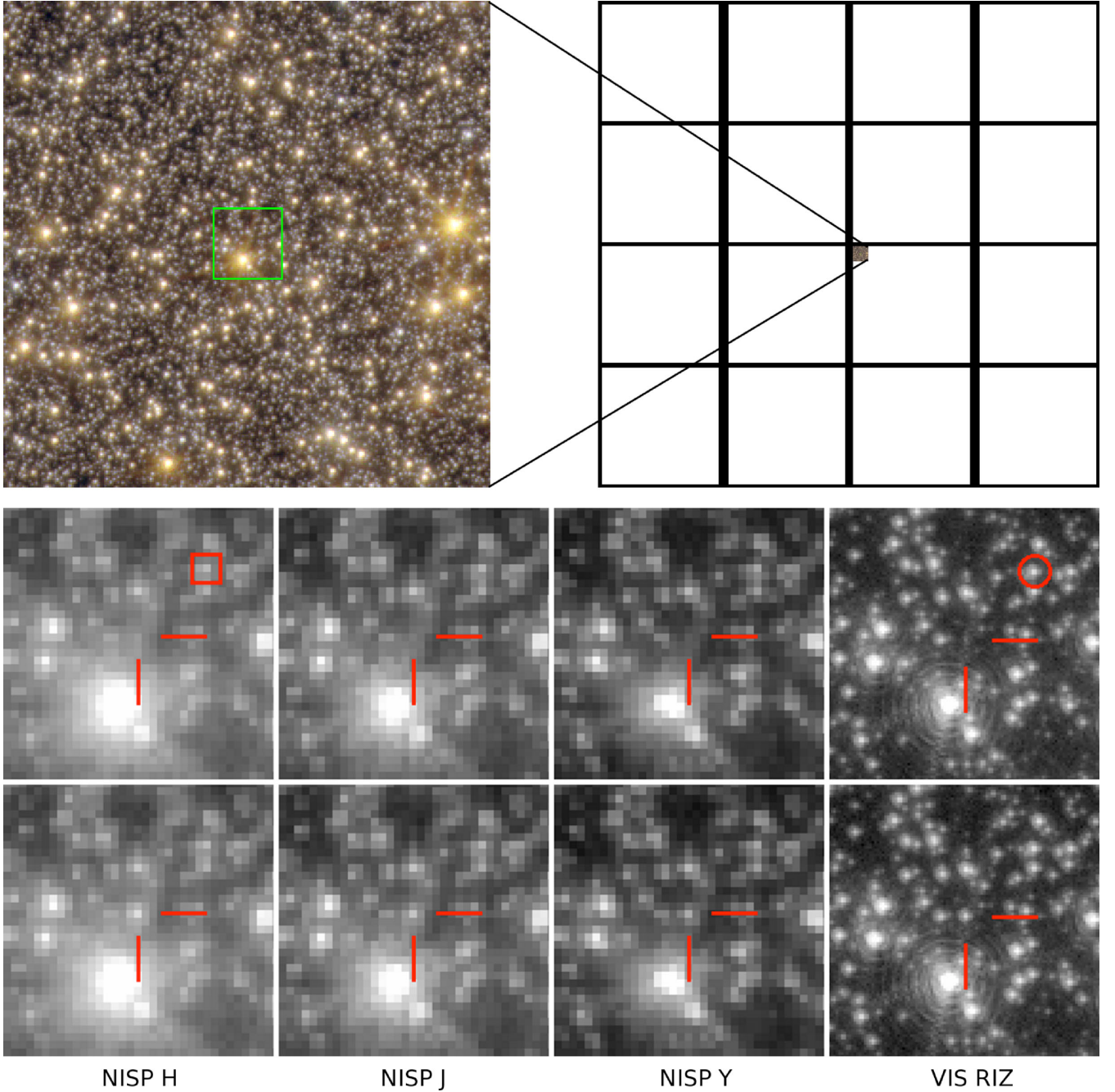


Figure 4. Top left: example of a simulated false-colour composite image of a typical star field from the *Euclid* MABμLS simulation, with colours assigned as red–NISP *H*, green–NISP *J* and blue–VIS *RIZ*, each with a logarithmic stretch. The light green box surrounds the region that is shown zoomed-in in lower panels. The image covers $77 \text{ arcsec} \times 77 \text{ arcsec}$, equivalent to $1/64$ of a single NISP detector, of which there are 16. These are shown to the right. Top right: approximate representation of the NISP instrument ‘paw-print’. The white areas show active detector regions, while black areas show the gaps between detectors. In the corner of one of the detectors is shown the size of a simulated image relative to the detectors. Bottom panels: the bottom panels show a small image region surrounding a microlensing event (located at the centre and marked by cross-hairs), the top row showing images at baseline and the bottom row showing images at peak magnification $\mu = 28$. The panels from left to right show NISP *H*, *J*, *Y* and VIS *RIZ* images, respectively. The small red box and red circle show the size of the aperture that was used to compute photometry in the NISP and VIS images, respectively.

efficiency, only a small image segment, just bigger than the largest aperture, is simulated in the standard operation of MABμLS.

4.6 Planet detections

To determine whether a bound planet is detected in a microlensing event we use three criteria, which will be further explained below:

- (i) the $\Delta\chi^2$ between the best-fitting single-lens model and the best-fitting planetary model must be greater than 160,
- (ii) the $\Delta\chi^2$ contribution from the primary observing band must be at least half of the total $\Delta\chi^2$,
- (iii) the time of closest approach between the lens star and the source (t_0) must be within one of the 30-d observing seasons.

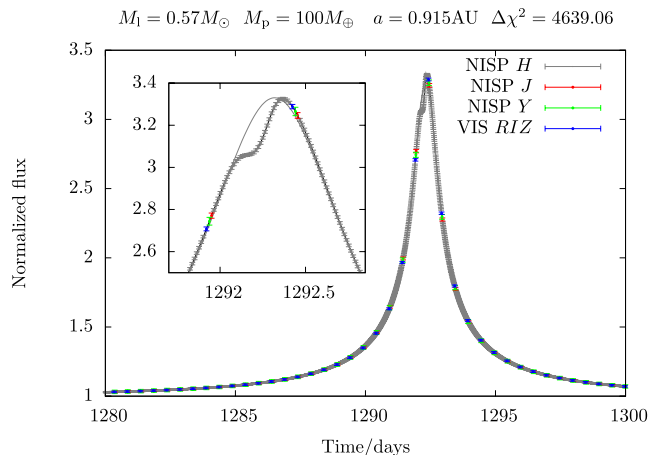


Figure 5. Light curve of the simulated event shown in Fig. 4. Fluxes are plotted normalized to the baseline and blending in the H band. Grey, red, green and blue show data from NISP H , J , Y and VIS RIZ , respectively. The event reaches a peak magnification of ~ 28 , but the normalized flux only increases by a factor of ~ 3.3 because the source ($H_{AB} = 20.9$) is blended with the diffraction spike of a much brighter star about 10 NISP-pixels away, and several other fainter stars, including the lens ($H_{AB} = 32.0$). At baseline the source contributes just 8 per cent of the total flux in the H -band photometry aperture, though in the RIZ -band aperture it contributes about 18 per cent. Some of the event parameters are shown above the figure: M_1 is the host-star mass; $\Delta\chi^2$ is introduced in the next section. The inset shows the peak of the event, where a planetary signature is clearly detected, relative to the single-lens light curve (grey line) that would have been observed were the planet not present. Data points are not scattered for clarity.

For the first criterion, we assume the best-fitting planetary model to be the true underlying model that was used to simulate the event. The $\Delta\chi^2$ with respect to the single-lens model was computed by fitting a point-source or finite-source single lens model as appropriate as described in Section 4.3. We choose $\Delta\chi^2 > 160$, which corresponds to a $\sigma > 12.6$ detection of the planet, because we find that the signatures of low-mass planets at this level of significance can usually be seen as systematic deviations from a single-lens light curve by eye [see e.g. event (c) in Fig. 7 below]. This is in contrast to Gould et al. (2010), who choose a higher threshold $\Delta\chi^2 > 500$ for planets in high-magnification microlensing events. Gould et al. (2010) were analysing data from multiple, small ground based observatories, which can suffer from various systematic effects (e.g. due to weather, differences in instrumentation, atmospheric effects in unfiltered data, etc.) that make the accurate estimation of photometric uncertainties, and hence also χ^2 , extremely difficult. More recent work by Yee et al. (2012) suggests that while a threshold of $\Delta\chi^2 > 500$ may be appropriate for planets in high-magnification events, a lower threshold of $\Delta\chi^2 \gtrsim 200$ is likely to be more appropriate for ground-based detection of planets in standard microlensing events, where the planetary signal is less ambiguous than in high-magnification events. A space-based microlensing data set will be much more uniform than ground-based data and will have much better characterized systematic effects, especially in the case of *Euclid*, whose design is driven by difficult, systematics-limited, weak-lensing galaxy shape measurements. In order to see if planetary parameters could be measured from $\Delta\chi^2 \approx 160$ light curves, we fitted a few simulated light curves using a Markov Chain Monte Carlo minimizer and found that even with $\Delta\chi^2 \approx 100$ it was still possible to robustly measure the basic microlensing event parameters, including the mass ratio, separation and in events where it

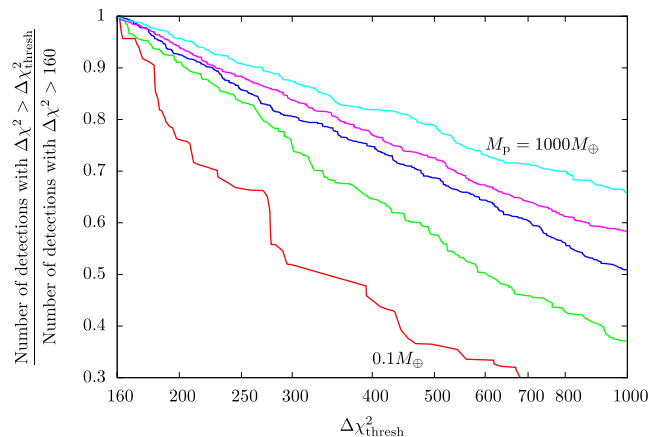


Figure 6. The effect of changing the $\Delta\chi^2$ threshold on the number of planet detections. The number of planet detections with a $\Delta\chi^2$ threshold $\Delta\chi^2_{\text{thresh}}$, relative to the number of detections with $\Delta\chi^2 > 160$, is plotted against $\Delta\chi^2_{\text{thresh}}$. The red, green, blue, magenta and cyan lines show the number of detections for 0.1-, 1-, 10-, 100- and 1000- M_{\oplus} planets, respectively.

was important, the source radius crossing time (see appendix A of Penny 2011).

Our choice of $\Delta\chi^2 > 160$ also aids comparison with other simulations which have chosen the same threshold (Bennett & Rhie 2002; Gaudi et al. unpublished), and is also the value adopted by the *WFIRST* science definition team for their calculations of the exoplanet figure of merit (Green et al. 2011). Despite the widespread adoption of $\Delta\chi^2 > 160$ as a threshold for planet detections in space-based microlensing surveys, it is worth considering the effect of changing the threshold. Fig. 6 plots the number of detections with $\Delta\chi^2$ greater than a variable threshold $\Delta\chi^2_{\text{thresh}}$, relative to our chosen threshold of 160. A higher $\Delta\chi^2$ threshold of $\Delta\chi^2_{\text{thresh}} = 200$ would reduce yields by only ~ 25 per cent for Mars-mass planets and less than ~ 10 per cent for higher mass planets. Even an extremely conservative threshold $\Delta\chi^2_{\text{thresh}} = 500$, such as used by Gould et al. (2010) for ground-based observations, reduces detections by 40–20 per cent, depending on planet mass, above $1 M_{\oplus}$. Such a reduction in yield would not prevent *Euclid* from probing the abundance of Earth-mass planets, but may significantly affect measurements for Mars-mass planets. However, such an extremely conservative cut will almost certainly not be necessary.

Returning to the definition of selection criteria, the second criterion is chosen in order to allow fair comparisons between the different bands that *Euclid* can observe in. By requiring that the contribution to $\Delta\chi^2$ from the primary observing band is at least half of the total $\Delta\chi^2$, we ensure that the primary band provides most of the information about the planet, and do not count as detections events where a planet is detected but most of the data are lost (e.g. due to saturation) or provides little information.

The final criterion is chosen to increase the chance that the microlensing event time-scale is well constrained. The season length for microlensing observations on *Euclid* will be short, ~ 30 d, due to the restrictions of the spacecraft’s sunshield. This can result in only a small portion of longer time-scale events being monitored, and may also mean that the event time-scale cannot be constrained. To first order, it is the ratio of the time-scale of the planetary perturbation to the time-scale of the main microlensing event which is used to measure the planetary mass ratio. Without the denominator of the ratio, the planetary mass ratio, and hence planetary mass cannot be estimated. Note however that it may be possible to constrain the

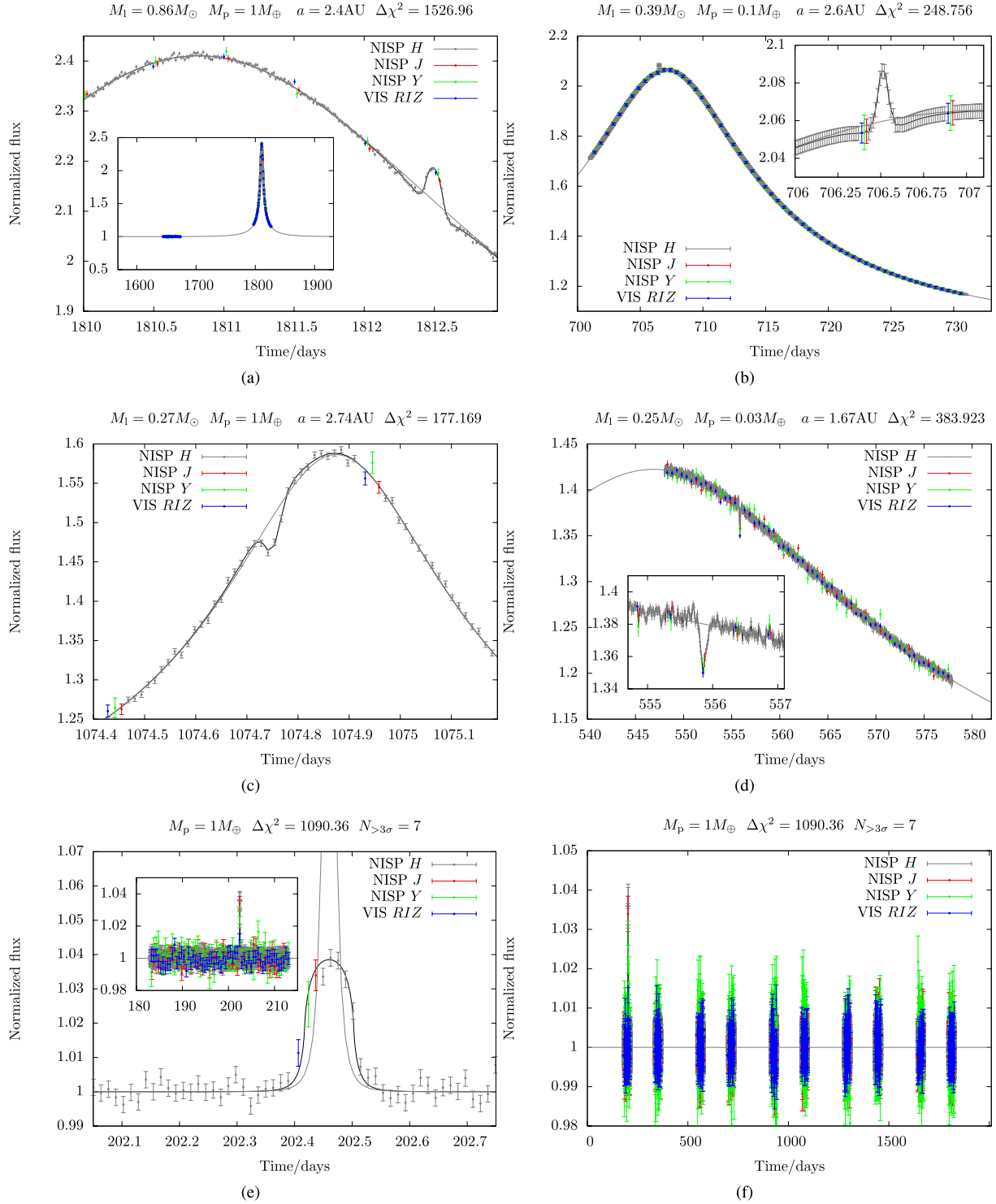


Figure 7. Example of light curves from the MAB μ LS simulation of ExELS. The left-hand column shows Earth-mass planet detections, with (a) showing a strong detection, (c) showing a detection close to the $\Delta\chi^2$ threshold and (e) showing an Earth-mass free-floating planet detection. (f) shows the full light curve of the free-floating planet detection in (e). The light curve in (b) shows a Mars-mass planet detection, but with the data points not scattered about the planetary light curve in order to emphasize the relative sizes of the photometric error bars. The light curve in (d) shows a $0.03\text{-}M_\oplus$ planet that causes a signal well above our $\Delta\chi^2$ threshold, but which is not counted as a detection because we require that the time of lens–source closest approach (the peak of the primary lensing event) be within an observing season. The inset figures, where included, either zoom in on planetary features or zoom out to show a larger section of the light curve. The grey, red, green and blue points with error bars show the simulated photometric data, while the black line shows the true light curve and the grey line shows the point-source single-lens light curve that would be seen if the planet were not present. Note that this single-lens light curve is not the same as the best-fitting single-lens light curve used to compute $\Delta\chi^2$. In (e) the grey curve shows the light curve that would be seen if the source were a point, not a finite disc as is actually the case. In each light curve, the flux has been normalized to the H -band flux, taking into account blending. The host mass, planet mass and semimajor axis, and $\Delta\chi^2$ are shown above each light curve.

event time-scale from the curvature of the light curve without the peak, as in event (d) shown in Fig. 7.

Fig. 7 shows some example light curves from the simulation. The light curves show planet detections with varying degrees of significance, ranging from a detection that narrowly passed the $\Delta\chi^2$ cut (light curve (c), $\Delta\chi^2 = 177$) to a very significant detection [light curve (a), $\Delta\chi^2 = 1527$]. Note, however, that many events will have much higher $\Delta\chi^2$ than this, up to $\Delta\chi^2 \approx 10^6$. The example light curves also cover a range of host and planet masses; the event with the lowest mass planet is event (d), which has a planet mass $M_p = 0.03 M_\oplus$ and detected with $\Delta\chi^2 = 384$; however, due to our second criterion that t_0 must lie in an observing season, this event is not counted as a detection.

4.6.1 Free-floating planets

To determine the expected number of free-floating planet detections we adopt similar detection criteria to those of Sumi et al. (2011). We require that in order to be classed as a detection, a free-floating planet light curve must have:

- (i) at least six consecutive data points (in any band) detected at greater than 3σ above baseline and
- (ii) $\Delta\chi^2 > 500$ relative to a constant baseline model, using all the data points in the primary observing band that satisfy the first criteria.

These criteria are in fact far more stringent than the corresponding criteria imposed by Sumi et al. (2011), but we chose them to remain conservative, as we do not impose other criteria relating to the quality of microlensing model fits and images that Sumi et al. (2011) use.

5 EXPECTED YIELDS

In this section, we discuss the results of the MAB μ LS simulations of ExELS. Unless otherwise noted, we present the results assuming that each lens star in the simulation is orbited by a single planet of mass M_p with semimajor axis in the range $0.03 < a < 30$ au.

Fig. 8 shows the expected number of planet detections plotted against planet mass, using a naive assumption that there is one planet of mass M_p and semimajor axis $0.03 < a < 30$ au per star. The error bars on this plot, and all subsequent plots of the yield, show the uncertainty due to the finite number of events that we simulate. Error bars are not shown for the free-floating planet simulation as they are similar to or smaller than the line thickness. For this naive assumption, we expect a *Euclid* planetary microlensing survey would detect ~ 8 , 38 and 147 bound Earth-, Neptune- and Saturn-mass planets (within 1-decade wide mass bins), and roughly half as many free-floating planets of the same masses. *Euclid* is sensitive to planets with masses as low as $0.03 M_\oplus$, but the detection rate for such low-mass planets is likely to be small unless the exoplanet mass function rises steeply in this mass regime.

Recent measurements of planet abundances using several techniques have shown that the often used logarithmic planet mass function prior is quite unrealistic. Multiple studies have suggested that the number of planets increases with decreasing planet mass (Cumming et al. 2008; Johnson et al. 2010; Sumi et al. 2010; Mayor et al. 2011; Cassan et al. 2012; Howard et al. 2012) and that planets are not distributed logarithmically in semimajor axis (Cumming et al. 2008). This picture is also supported by planet population synthesis models (Ida & Lin 2008; Mordasini, Alibert & Benz 2009a;

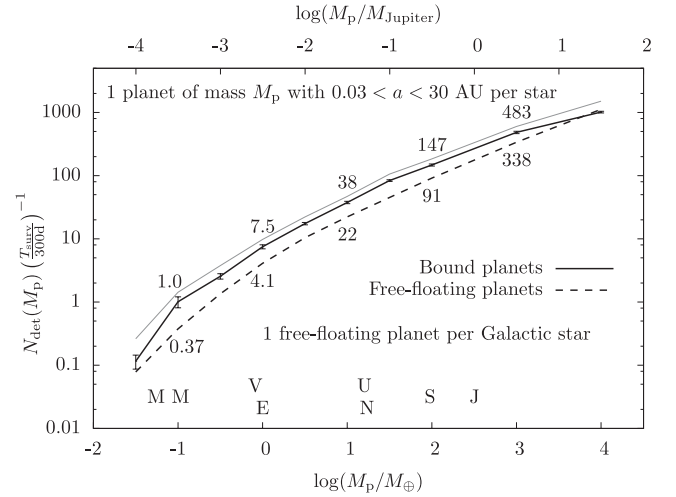


Figure 8. Number of planets detected in a 300-d survey by *Euclid*, plotted against planet mass M_p . The survey is primarily conducted in the NISP *H* band. The solid black line shows the expected bound planet yield, assuming one planet of mass M_p per star with semimajor axis $0.03 \leq a < 30$ au; error bars show our estimated statistical errors from simulations of a finite number of light curves. The solid grey line shows the yield if the third cut on the time of the event peak is not applied. The dashed line shows the expected yield of free-floating planets, assuming there is one free-floating planet per Galactic star. The masses of Solar system planets are indicated by letters, and the numbers above/below the lines show the yields when applying the full sets detection criteria.

Mordasini et al. 2009b). In Fig. 9, we consider a more realistic two-parameter power-law planetary mass function:

$$f(M_p) \equiv \frac{d^2 N}{d \log M_p d \log a} = f_\bullet \left(\frac{M_p}{M_\bullet} \right)^\alpha, \quad (8)$$

where $f(M_p)$ is now the number of planets of mass M_p per decade of planet mass per decade of semimajor axis per star and where f_\bullet is the planet abundance (in $\text{dex}^{-2} \text{ star}^{-1}$) at some mass M_\bullet about which the mass function pivots. Here, α is the slope of the mass function, with negative values implying increasing planetary abundance with decreasing planetary mass. For simplicity, and because there are no measurements of the slope of the planetary semimajor axis distributions in the regime probed by microlensing, we assume that $dN/d \log a$ is constant.

We use two estimates of the mass-function parameters based on measurements made using both RV and microlensing data sets. The first, more conservative mass function (in terms of the yield of low-mass planets) uses the mass-function slope $\alpha = -0.31 \pm 0.20$ measured by Cumming et al. (2008) from planets with periods in the range $T = 2\text{--}2000$ d, detected via RV. For the normalization, we use $f_\bullet = 0.36 \pm 0.15$ at $M_\bullet \approx 80 M_\oplus$, measured by Gould et al. (2010) from high-magnification microlensing events observed by Microlensing Follow-up Network (MicroFUN). Gould et al. (2010) argue that this value is consistent with the abundance and semimajor axis distribution measured by Cumming et al. (2008), extrapolated to orbits with $a \approx 2.5$ au. We note that the host stars studied by Cumming et al. (2008) typically have higher masses than those that are probed by microlensing. We call the combination of the Cumming et al. (2008) slope and Gould et al. (2010) normalization, the RV mass function. The second mass function we consider has a mass function slope $\alpha = -0.73 \pm 0.17$ and normalization $f_\bullet = 0.24^{+0.16}_{-0.10}$ at $M_\bullet = 95 M_\oplus$, as measured by Cassan et al. (2012) from microlensing detections. We call this

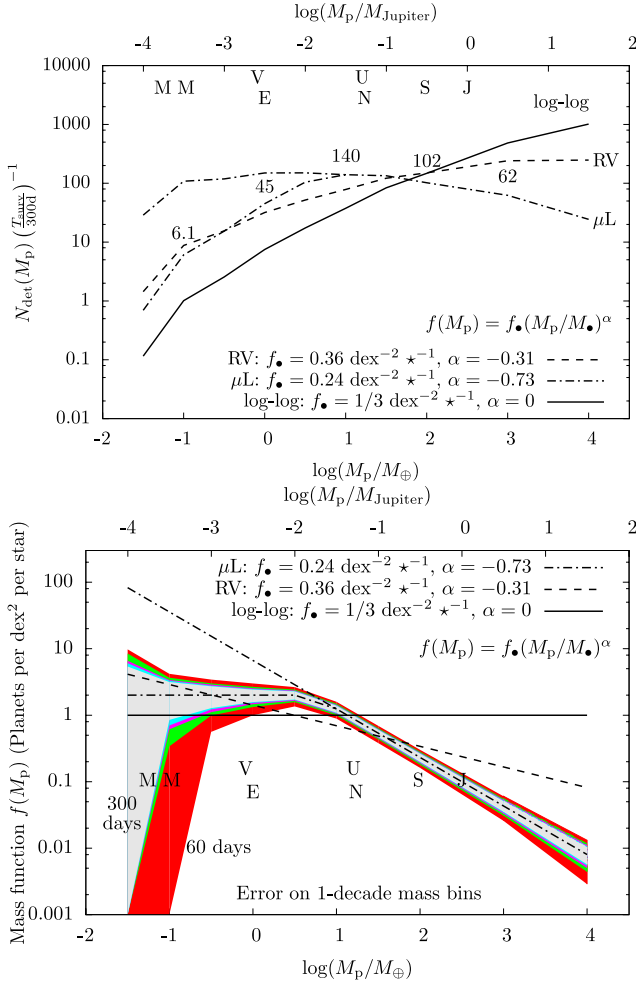


Figure 9. The upper panel shows predictions of the planet yield based on recent estimates of the planet abundance and planet-mass distribution. The solid line shows a naive logarithmic prior of one planet per decade of mass and semimajor axis per star. The dashed line (labelled RV) shows the expected yield using an extrapolation of the mass-function slope measured by Cumming et al. (2008) using RV data combined with a normalization measured by Gould et al. (2010) from microlensing data, which Gould et al. (2010) argue is compatible with the slope of the semimajor axis distribution found by Cumming et al. (2008). The dot-dashed line (labelled μL) shows the expected yield using the mass-function slope and normalization measured from microlensing data by Cassan et al. (2012). A branching dot-dashed line, and the numbers above it, show the yield if the Cassan et al. (2012) microlensing mass function saturates at two planets per dex^2 per star. The lower panel shows the actual form of each of the mass functions shown in the top panel. The filled, coloured regions show the size of model-independent 1σ statistical (square root N) errors on measurements of the planet abundance in 1-decade mass bins centred at M_p , assuming the saturated microlensing mass function and also assuming that only half of the planet detections have host mass measurements. The red, green, magenta, cyan and grey regions show the error bars for *Euclid* microlensing surveys lasting 60, 120, 180, 240 and 300 d, respectively. This implies a 300-d *Euclid* microlensing survey would measure the abundance of Earth-mass and Mars-mass planets to approximately 4.7 and 1.7 σ , respectively, whereas a 120-d *Euclid* survey would reach just 3.0 and 1.2 σ significance, both assuming the saturated mass function.

the microlensing (μL) mass function. We note that at low masses, the extrapolation of the microlensing mass function implies close packing of planetary systems. We also plot the microlensing mass function assuming that it saturates at a planet abundance of 2 dex^{-2}

Table 3. Expected total number of planet detections by a 300-d *Euclid* microlensing survey for different mass functions (with planet masses in the range $0.03 < M_p/M_\oplus < 3000$ (roughly 0.6 Mercury-mass to 10 Jupiter-mass)).

Mass function	Number of detections
log-log	718
RV	502
μL	541
μL saturated	356

star^{-1} . However, we note that the Kepler 20 planetary system comprises five exoplanet candidates so far (Gautier et al. 2012), all within about 1 dex in both mass and separation. Our saturation limit is therefore likely to be conservative.

Fig. 9 plots the yields that would be expected for the different mass functions. Perhaps the most important thing that the top panel of Fig. 9 highlights is that, despite the degree of uncertainty in the extrapolation to low planet masses provided by empirical estimates of the mass functions, we can expect a 300-d *Euclid* survey to detect significant numbers of planets of Mars-mass and above. Table 3 shows the total number of detections expected for each mass function. The number of expected detections imply that *Euclid* data would allow the different model mass functions to be discriminated between. In fact, we can look at the power of *Euclid* to measure the mass function more easily in the lower panel of Fig. 9.

The lower panel of Fig. 9 shows the expected uncertainty on the planet abundance in one-decade mass bins, assuming the saturated microlensing mass function and that half the *Euclid* planet detections have mass measurements. Such mass measurements can be made by estimating the mass of the host from photometry of the host star. Such an estimate should be possible for many of the hosts using ExELS survey data alone, thanks to the extremely deep, high-resolution images that can be built by combining the randomly dithered survey images. A stack of such images, one for each season, will allow the light of the source, host and any unrelated stars to be disentangled as they separate due to their mutual proper motions. Bennett, Anderson & Gaudi (2007) give a detailed discussion of how these mass measurements are made. Bennett et al. (2007) estimate that such mass measurements should be possible in most space-based planetary microlensing detections. However, it may be the case that the larger pixels of the NISP instrument preclude full photometric host-mass measurements, but even if this is so, the deep, high-resolution images from the VIS channel should provide constraints. Even without mass measurements, Fig. 9 indicates the precision of measurements of the mass-ratio function, which would encode much of the same information. The uncertainties shown by the coloured bands in the figure are the uncertainty on the absolute abundance of planets in each bin. This is in contrast to measurements such as those of Cumming et al. (2008) and Cassan et al. (2012), which are the uncertainties on a small number of power-law model parameters *assuming* the models are correct. If we here assume that the saturated microlensing mass function is correct, then we can see that a 300-d *Euclid* microlensing survey would measure the abundance of Earth-mass planets to be 2 per star with a significance of 4.7 σ , and similarly the abundance of Mars-mass planets to 1.7 σ . However, if the microlensing programme were only 120 d, the significance of the abundance measurements would reduce to 3.0 and 1.2 σ for Earth- and Mars-mass planets, respectively.

5.1 The M_p – a diagram

We have discussed the ability of our simulated survey to probe the planetary mass function, but a perhaps more important goal of such a survey is to explore the planet mass–semimajor axis (M_p – a) plane where planet formation models predict a lot of structure (e.g. Ida & Lin 2004; Mordasini et al. 2009a). Fig. 10 plots contours of planet detection yields for the simulated survey in the M_p – a plane, assuming there is one planet per host at a given point in the plane. The positions of planet detections to date, by all detection methods (RV, transits, direct detection, timing and microlensing) are also shown, as well as candidate planets detected by *Kepler* (Batalha et al. 2013), which have been plotted by assuming the planetary mass–radius relation, $M_p = (R_p/R_\oplus)^{2.06} M_\oplus$, which is used by Lissauer et al. (2011). It is clear that microlensing surveys probe a different region of the M_p – a plane to all other detection methods, covering planets in orbits ~ 0.2 –20 au, as well as free-floating planets. Note that microlensing can be used to detect planets with any semimajor axis larger than ~ 20 au, but there is a significant chance that the microlensing event of the host will not be detectable. These cases will be classified as free-floating planet detections (see e.g. Sumi et al. 2011; Bennett et al. 2012). The peak sensitivity of the simulated *Euclid* survey is at a semimajor axis $a \approx 1.5$ –5 au, in good agreement with previous simulations of space-based microlensing surveys (Bennett & Rhie 2002; Gaudi et al. unpublished). The planets to which *Euclid* is sensitive lie in wider orbits than those detectable by *Kepler*, and stretch to much lower masses than can be detected by RV in this semimajor axis range, reaching down to Mars mass. The range of semimajor axis probed by *Euclid* decreases with decreasing mass, from ~ 0.2 to more than 20 au for Jupiter-mass planets, down to ~ 1 –14 au for Earth-mass planets and ~ 1.5 –5 au for Mars-mass planets. There will be a significant degree of overlap between *Euclid* and full-mission *Kepler* detections at separations

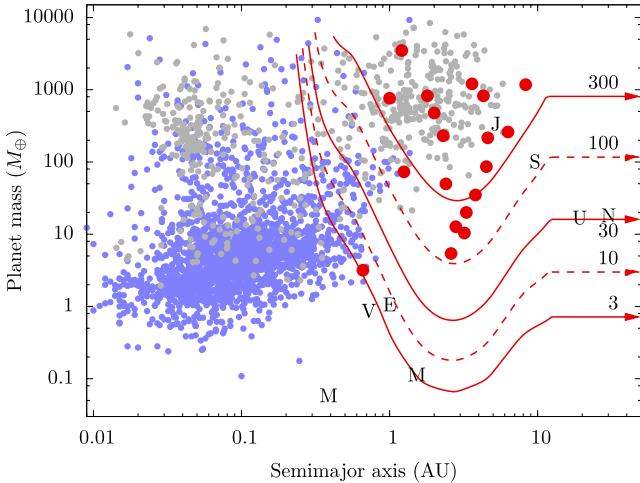


Figure 10. The sensitivity of *Euclid* in the M_p – a plane. The red lines show the expected yield of a 300-d *Euclid* survey with 60 d of observations per year, plotted against planet mass and semimajor axis, assuming one planet per star at each point in the planet mass–semimajor axis plane. Horizontal arrows are plotted when the expected yield of free floating planets of that mass exceeds the yield of bound planets (assuming one free-floating planet per star). The grey points show planets listed by the Exoplanets Orbits Database as of 2012 March 17th (Wright et al. 2011), and light blue points show candidate planets from the *Kepler* mission (Batalha et al. 2013), with masses calculated using the mass–radius relation of Lissauer et al. (2011). The red points show planets detected via microlensing to date.

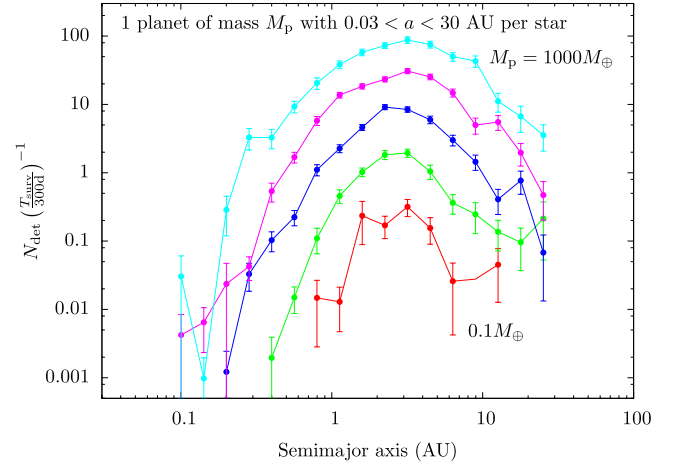


Figure 11. Predictions of the planet yield as a function of semimajor axis a . The red, green, blue, magenta and cyan lines denote yields for 0.1, 1, 10, 100 and 1000 M_\oplus , respectively.

$0.3 \lesssim a \lesssim 1$ au. Similarly, at masses larger than $M_p \gtrsim 50 M_\oplus$, there will be overlap with RV surveys over a wide range of semimajor axes. Both overlaps will facilitate comparisons between the data sets of each technique. It should be noted, however, that the host populations probed by each technique are different, as we will see in the next section.

Fig. 11 plots the expected yield for various planet masses as a function of semimajor axis a , using a simplistic assumption of one planet per host at the given mass and separation. The peak sensitivity of *Euclid* is to planets with semimajor axis $a \approx 1.5$ –5 au. The sensitivity is ~ 10 per cent of the peak sensitivity in the range $0.5 \lesssim a \lesssim 20$ au.

Fig. 12 plots the distribution of planet detections as a function of the effective temperature of the planet, calculated as

$$T_{\text{eff},p} = \sqrt{\frac{R_1}{2a}} (1 - A)^{1/4} T_{\text{eff},1}, \quad (9)$$

where R_1 is the radius of the host star, A is the planet’s albedo, assumed to be $A = 0.3$ and $T_{\text{eff},1}$ is the effective temperature of the star. Both R_1 and $T_{\text{eff},1}$ are provided as outputs of the Besançon. The distribution of detected planet temperatures peaks at ~ 50 –80 K, with a long tail towards lower temperatures and a rapid decline

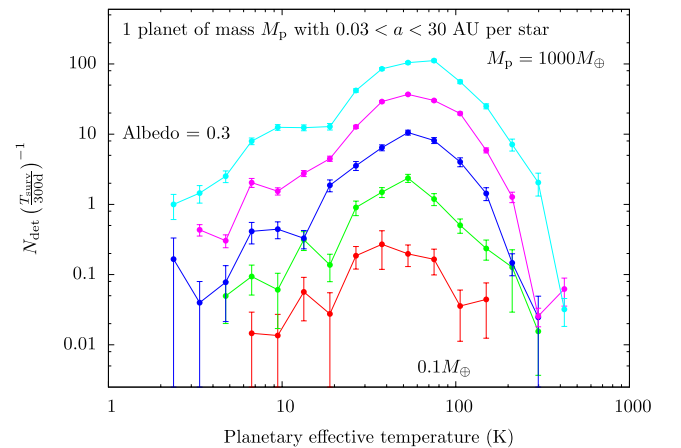


Figure 12. The number of planet detections plotted against the planetary effective temperature, assuming an albedo of 0.3. Lines are as for Fig. 11.

towards higher temperatures. However, there should still be a small number of detections of planets with effective temperatures $\gtrsim 200$ K.

5.2 Host-star properties

The primary observable of the microlensing light curve that is related to the host-star's mass is the event time-scale. The time-scale is a degenerate combination of the total lens mass, the relative lens–source proper motion and the distances to the source and lens. Fig. 13 plots the time-scale distributions of all the microlensing events that occur within the observed fields and also the distributions for several cases of planet detections. The time-scale distribution for bound planet detections is similar to the underlying time-scale distribution, but is affected by the choice of detection criteria. Our third criterion, designed to select only events with well-characterized time-scales, cuts out potential detections in some long time-scale events. Some of these events are detections of planets with large orbits, where the planetary lensing event is seen but the stellar host microlensing event is only partially covered (in which case the planet parameters may be poorly constrained) or may be missed completely (in which case the planet event would enter the free-floating planet sample). However, in other cases the cut on t_0 is too zealous, and long time-scale events with t_0 outside the observing window, but with significant magnification in several seasons, are cut from the sample. The time-scale of these events, and hence also the planetary parameters, are likely to be well constrained.

Fig. 13 also plots the free-floating planet time-scale distributions for planets of 1 and $100 M_{\oplus}$. Free-floating planets will dominate

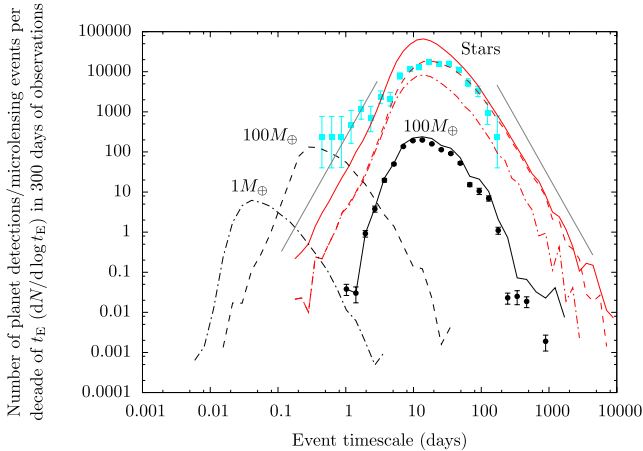


Figure 13. The distribution of microlensing time-scales. The red curves show the distribution of event time-scales for stellar microlensing events. The solid curve shows all events with impact parameter $u_0 \leq 1$, regardless of whether they are detected, the dashed curve shows events which are detected above baseline with $\Delta\chi^2 > 500$, and the dot-dashed curve shows those detected events which peak during an observing season. The solid grey lines show the theoretically expected asymptotic slope of the distribution, with power law slopes of ± 3 (Mao & Paczyński 1996). The cyan data points show the time-scale distribution observed by the MOA survey (Sumi et al. 2011), which is uncorrected for detection efficiency and scaled arbitrarily – this is most closely comparable to the dashed line showing all events detected by *Euclid*. The black lines and data points show the time-scale distribution for events with detected planets. The solid line shows the time-scale distribution of the host-star microlensing event for $100 M_{\oplus}$ planet detections with no restriction on t_0 , while the data points show the same, but only for events where t_0 lies in an observing season. The dashed and dot-dashed lines show the time-scale distribution of detected $100 M_{\oplus}$ and $1 M_{\oplus}$ free-floating planet detections, respectively.

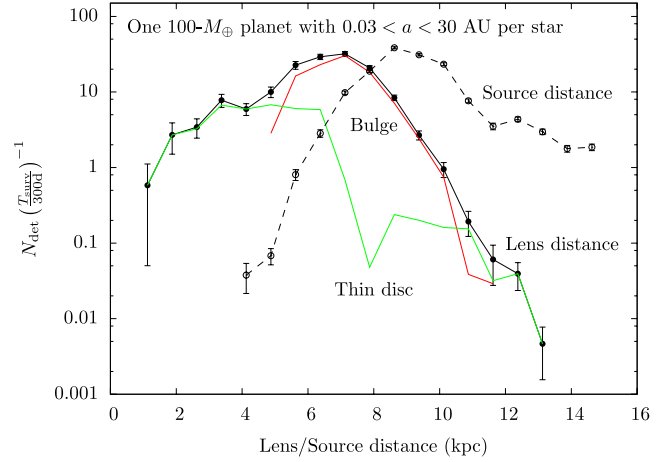


Figure 14. Predictions of the $100 M_{\oplus}$ planet yield as a function of lens (solid lines) and source (dashed line) distances, D_l and D_s , respectively. The red and green lines show the contributions due to bulge and thin disc lenses, respectively; thick disc and halo lenses contribute the remainder, which is small.

the time-scale distribution at time-scales less than a few days, if they exist in numbers similar to those suggested by Sumi et al. (2011), which is twice the abundance that we have assumed.

Fig. 14 plots the distribution of $100 M_{\oplus}$ planet detections as a function of lens and source distances, D_l and D_s , respectively. The contribution of thin-disc and bulge populations to the yields is also plotted. Thick disc and stellar halo lens yields have not been plotted as at no point are they dominant. However, near the Galactic Centre it should be noted that stellar halo lenses have a higher yield than the thin disc due to the disc hole (see Section 4.1). Most of the host stars are near-side bulge stars between $5.5 < D_l < 8$ kpc. Beyond this, the number of lenses with detected planets drops off exponentially with increasing distance, dropping by four orders of magnitude from $D_l \sim 9$ to 15 kpc. The steepness of this fall is partly caused by the truncation of the source distribution at 15 kpc. Though the majority of lenses are in the bulge, a substantial number reside in the near disc. The contribution of planet detections by each component is 68, 27, 1.2 and 3.5 per cent for the bulge, thin disc, thick disc and stellar halo populations, respectively. Unlike the lens stars, the majority of source stars reside in the far bulge, with a small fraction in the far disc. Very few near disc stars act as sources due to the low optical depth to sources on the near side of the bulge.

Fig. 15 plots the distribution of $100 M_{\oplus}$ planet detections as a function of the host-star spectral type. The majority of hosts are M dwarfs, but there are a significant number of detections around G and K dwarfs and also white dwarfs. There will be a negligible number of detections around F and earlier type stars due to their low number density. The distribution of planetary host stars probed by *Euclid* is very different to that probed by any other technique. For example, most of *Euclid*'s host stars are M dwarfs in the bulge, whereas most of *Kepler*'s host stars are FGK dwarfs in the disc (Howard et al. 2012).

6 VARIATIONS ON THE FIDUCIAL SIMULATIONS

In the previous section, we have investigated the potential planet yield of a *Euclid* microlensing survey and the properties of detectable planets and their hosts. In this section, we investigate how the planet yield is affected by our choice of primary observing

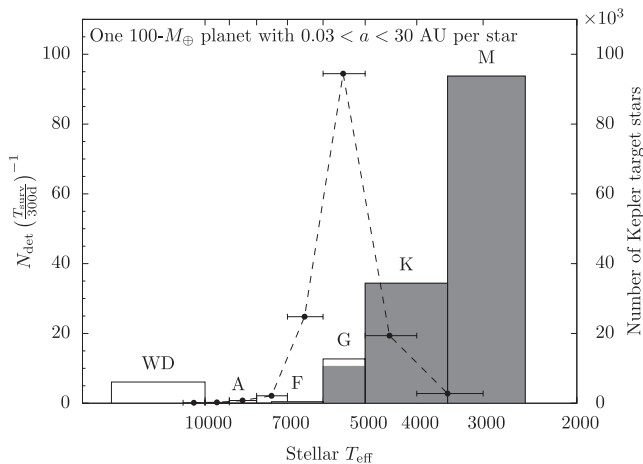


Figure 15. Histogram of the number of $100\text{-}M_{\text{Jup}}$ planet detections plotted against the effective temperature of the host star, binned according to the spectral type designations in the Besançon model. The shaded region shows the contribution due to main-sequence host stars, while white regions show the contribution of evolved host stars. The dotted line shows the distribution of effective temperatures of high-priority Kepler target stars (Batalha et al. 2010).

band, the level of systematic photometry errors and the choice of spacecraft design.

6.1 Primary observing band

We begin by examining the choice of primary observing band. The survey strategy we have simulated involves the majority of observations being taken in a primary band with a cadence of ~ 18 min while auxiliary observations to gain colour information are taken every ~ 12 h. We consider the use of each band available to *Euclid*, Y , J and H in the near-infrared using NISP and RIZ using VIS. As NISP and VIS can image the same field concurrently we also consider simultaneous observations in RIZ and H . To maintain a comparable cadence, when RIZ is the primary band (or VIS is operating simultaneously with NISP), the VIS exposure times are 270 s, as opposed to 540 s when RIZ is used as an auxiliary band. In each scenario, the total exposure time is identical, but the actual cadence is slightly different due to differences in the number of stacked images (we assume a 5 s overhead between the images in the NISP stacks, and the shutter on VIS takes 10 s to open or close). As the sensitivities of the instruments in each band are slightly different, the images have different depths.

Fig. 16 shows the expected planet yields as a function of the primary observing band. Focusing first on the scenarios without simultaneous imaging, it is clear that H band offers the highest planet yields compared to the other two infrared bands. This is partly due to the increased depth from a stack of five images for H as opposed to a stack of three images for J and Y (the individual exposure times have been chosen to optimize *Euclid*'s cosmological surveys; Laureijs et al. 2011). However, it is also due to the lower extinction suffered in the H band, and the correspondingly higher number density of sources with magnitudes lower than the source catalogue cutoff of $H_{\text{vega}} < 24$.

The survey imaging with both available instruments simultaneously obviously performs better than when using each instrument on its own. The increase in yield is $\sim 22 \pm 4$ per cent for both Saturn-mass and Earth-mass planets. As for the single primary instrument scenarios, we require that the $\Delta\chi^2$ contribution of the primary bands

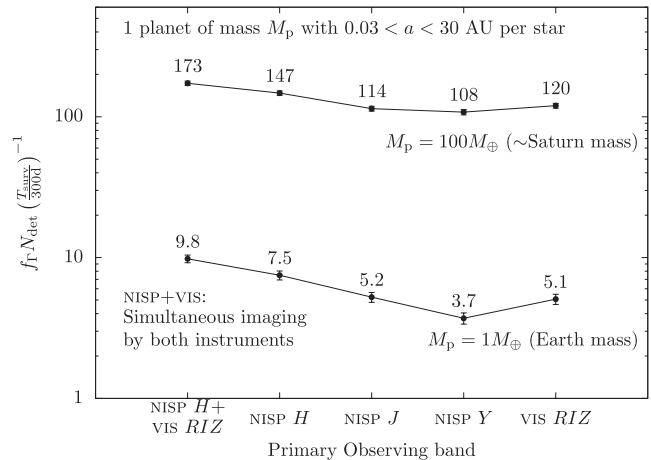


Figure 16. Expected planet detections plotted against the different primary observing bands. Free-floating planet detections are not included.

(the sum of RIZ and H) to be greater than half the total $\Delta\chi^2$. In reality, the expected yield of the simultaneous imaging scenario represents an upper limit, as there are a number of limitations that may preclude simultaneous imaging with VIS for all pointings. These include losses due to cosmic rays, which will affect ~ 20 per cent of VIS data points (Laureijs et al. 2011), downlink bandwidth and power consumption limitations, which may only allow a simultaneous VIS exposure every other pointing, say. The increase in yield may therefore be small. However, the real value of simultaneous VIS imaging will be the increased number of exposures it is possible to stack in order to detect the lens stars. This will greatly increase the depth of VIS images stacked over the entire season, which in turn will allow the direct detection of more lens stars, and hence an increase in the accuracy and number of mass measurements it is possible to make. We discuss this further in Section 7. Simultaneous VIS imaging will also allow source colours to be measured in many low-mass free-floating planet events, which will help to constrain their mass. It is clear therefore that as many simultaneous VIS exposures should be taken as possible.

6.2 Systematic errors

There are many possible sources of systematic error, which can include image reduction, photometry, image persistence in the detector, scattered light, temperature changes in the telescope and source and intrinsic variability in the source, lens or a blended star. The magnitude and behaviour of each systematic will also be different; for example, temperature changes will likely induce long-term trends in the photometry, while image persistence may introduce a small point-to-point scatter together with occasional, randomly timed outliers. It is likely that the systematics that produce long-term trends may be corrected for, to a large extent, either by using additional spacecraft telemetry or by detrending similar to that used in transiting exoplanet analyses (e.g. Holman et al. 2010). Even for some systematics that behave more randomly, it may be possible to account for and correct errors; for example, it may be possible to correct for image persistence errors to a certain degree by using preceding images. It is therefore difficult to predict the magnitude and behaviour of systematics a priori. We therefore choose to model systematic errors by assuming them to be Gaussian, and add the systematic component in quadrature to the standard photometric error. While likely a poor model for the actual systematics, it

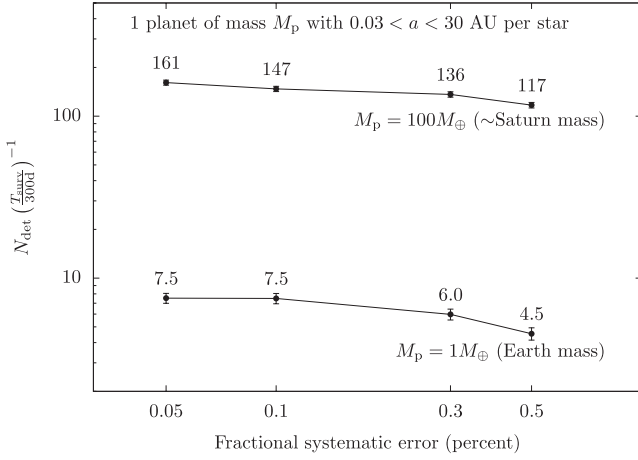


Figure 17. Expected planet detections plotted against the size of the systematic error component.

effectively introduces a floor below which it is not possible to improve photometry by collecting more photons.

Fig. 17 plots the expected planet yield against differing values of the systematic error component that we assume. In all other simulations, we have used the fiducial value of the fractional systematic error $\sigma_{\text{sys}} = 0.001$. Reducing the systematic error further from this point does not provide a significant increase in yield, as for the most part, at this level of systematic, photometric accuracy is limited by photon noise. Increasing the systematic to $\sigma_{\text{sys}} = 0.003$ does cause a drop in yields, by ~ 8 per cent for giant planets to ~ 20 per cent for low-mass planets, as the systematic component becomes comparable to the photon noise. The situation is worse still for $\sigma_{\text{sys}} = 0.005$, where the systematic component dominates. However, even with a systematic error component this large and the conservative log–log mass function, ~ 4 – 5 Earth-mass planet detections can be expected.

It is not possible at this stage to estimate the magnitude of systematic error that should be used in our simulations, but it should be noted that ground-based microlensing analyses often have systematic errors of a similar magnitude to the values that we have simulated (Bennett, private communication). The tight control of systematics required by *Euclid* for galaxy-shape measurements should mean that *Euclid*-VIS will be one of the best-characterized optical instruments ever built (Laureijs et al. 2011); similarly, NISP will be optimized for performing accurate, photometry of faint galaxies. Furthermore, Clanton et al. (2012) recently showed that the HgCdTe detectors that will be used in NISP can perform stable photometry to ~ 50 parts per million. How these considerations will relate to crowded-field photometry is not yet clear, but it is almost certain that the systematics will be lower than those achieved from the ground, potentially by a large factor. Our fiducial choice of a fractional systematic error 0.001 (1000 parts per million) is therefore almost certainly conservative.

6.3 Slewing time

Another uncertainty in the yields we predict results from uncertainties in the spacecraft design.

Whilst the manufacturer and final design for the *Euclid* spacecraft is yet to be decided it is possible to explore some factors which are likely to have an important bearing on its microlensing survey capabilities. One important factor is the choice of manoeuvring system used for slewing between fields. For fixed exposure and

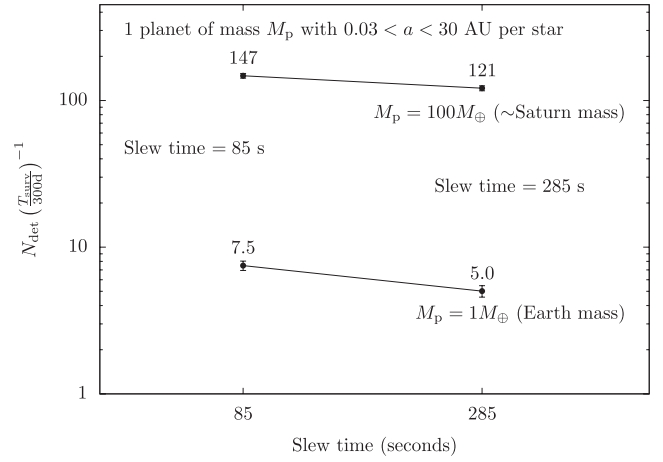


Figure 18. Expected planet detections plotted for 85 and 285-s slewing times, which encompass the likely range anticipated by different designs for the *Euclid* manoeuvring system.

areal coverage, the slew and settle time determines the cadence it is possible to achieve on a particular field. Alternatively, for larger slewing times one may shorten the exposure time to maintain cadence and areal coverage. Since the detection of low-mass planets depends crucially on cadence this alternative approach is preferable when considering the impact of adjustments to the slewing time.

The slew time will ultimately depend on the technology used, in particular whether gas thrusters or reaction wheels are used to perform field-to-field slews. A plausible range for the slew times based on initial design proposals is 85–285 s.

Fig. 18 shows the expected yield at either end of this slew time range. Maintaining a constant cadence of around 20 min between repeat visits to a given field allows 270 s per pointing of stacked *H*-band exposure time for 85-s slews and 108 s for 285-s slews. The increased depth allowed by a shorter slewing time produces a yield that is higher by 50 ± 12 per cent at Earth mass and 22 ± 5 per cent at Saturn mass.

7 SUMMARY DISCUSSION

The *Euclid* dark energy survey, which has been selected by ESA to fly in 2019, is likely to undertake additional legacy science programmes. The design requirements of the *Euclid* weak-lensing programme also make it very well suited to an exoplanet survey using microlensing and the *Euclid* Exoplanet Science Working Group has been set up to study this proposal.

We have developed a baseline design for the ExELs using a detailed simulation of microlensing. The simulator, dubbed MAB μ LS, is based on the Besançon Galaxy model (Robin et al. 2003). It is the first microlensing simulator to generate blending and event parameter distributions in a self-consistent manner, and it enables realistic comparisons of the performance of *Euclid* in different optical and infrared passbands. We have used MAB μ LS to study a design for ExELs with a total observing baseline of up to 300 d and a survey area of 1.6 deg^2 . We show that of the bandpasses available to *Euclid* a survey primarily conducted in *H* will yield the largest number of planet detections, with around 45 Earth-mass planets and even ~ 6 Mars-mass planets. These numbers are based on current extrapolations of the exoplanet abundance determined by microlensing and RV surveys. Such low-mass planets in the orbits probed by *Euclid* (all separations larger than ~ 1 au) are presently inaccessible to any

other planet detection technique, including microlensing surveys from the ground.

While space-based microlensing offers significantly higher yields per unit time than do ground-based observations, this is not the only motivation for space-based observations. A standard planetary microlensing event does not automatically imply a measurement of planet mass or semimajor axis, only the planet–star mass ratio and the projected star–planet separation in units of the Einstein radius r_E . To measure the planet mass, we must measure the lens mass, either by detecting subtle, higher order effects in the microlensing light curve, such as microlensing parallax (e.g. Gould 2000; An et al. 2002), or directly detecting the lens star (Alcock et al. 2001; Kozłowski et al. 2007). Without these the mass can only be determined probabilistically (e.g. Beaulieu et al. 2006; Dominik 2006). The projected separation in physical units can be determined if the lens mass and distance are known (as well as the source distance, which it is possible to estimate from its colour and magnitude). Determining the semimajor axis will require the detection of orbital motion (Bennett et al. 2010b; Skowron et al. 2011), but this will only be possible in a subset of events (Penny, Mao & Kerins 2011). For a survey by *Euclid*, we expect parallax measurements to be rare. Parallax effects are strongest in long microlensing events lasting a substantial fraction of a year due to the acceleration of the Earth (Gould 1992), but *Euclid*'s seasons will be too short to constrain or detect a parallax signal in most events (Smith et al. 2005).

However, thanks to the high-resolution imaging capabilities of the VIS instrument, lens detection should be common (Bennett et al. 2007). In events where the light of the lens is detected, the lens mass and distance can be determined by combining measurements of the angular Einstein radius θ_E (which gives a mass–distance relation) with a main-sequence mass–luminosity relation. Measurement of θ_E should be possible for a large share of detected events, either from finite-source effects in the light curve or by measuring the relative lens–source proper motion as the pair separates (Bennett et al. 2007). It is also possible to estimate the lens mass and distance from measurements of its colour and magnitude (Bennett et al. 2007). From a single epoch of NISP and VIS images, this will likely not be possible. However, over each 30-d observing period around 2000 images will be taken in NISP H band, with possibly a similar number with the VIS camera. These images will have random pixel dither offsets. The images can therefore be stacked to form a much deeper, higher resolution image in each band. From these images, it should be possible to isolate the source (whose brightness is known from the light curve) from any blended light. After subtracting the source, if the remaining light is due to the lens, its mass can be estimated from its colour and magnitude. The planet mass can then be determined, as the planet–host mass ratio is known from the light curve. However, if either the source or lens has a luminous companion, estimating the lens mass will be more difficult (Bennett et al. 2007).

We have not attempted to estimate the number of planet detections with mass measurements in this work, but we aim to study this in a future work. These calculations will allow a full determination of planetary microlensing figures of merit, such as the one defined by the *WFIRST* Science Definition Team (Green et al. 2011).

Finally, it is worth stating that our simulation of ExELS has not been optimized. There are many factors that can be varied to increase planet yields, such as the choice of target fields, the number of target fields and the strategy with which they are observed. However, planet yields are not the only measure of the scientific yield of the survey. For example, planetary-mass measurements without the need for additional follow-up observations would be an important

goal of the *Euclid* microlensing survey, and so any assessment of the relative performance of different possible surveys must also evaluate performances in this respect.

We have shown that ExELS will be unrivalled in terms of its sensitivity to the cold exoplanet regime. A survey of at least six months total duration should be able to measure the exoplanet distribution function down to Earth mass over all host separations above 1 au. This will fill in a major incompleteness in the current exoplanet discovery space which is vital for informing planet formation theories. This together with ExELS's ability to detect hot exoplanets and sub-stellar objects (Paper II) make it a very attractive addition to *Euclid*'s science capability.

ACKNOWLEDGEMENTS

We thank Mark Cropper and Gregor Siedel for providing the VIS and NISP PSFs. The computational element of this research was achieved using the High Throughput Computing facility of the Faculty of Engineering and Physical Sciences, The University of Manchester. MTP acknowledges the support of an STFC studentship. We are grateful to Scott Gaudi, Dave Bennett, David Nataf and Andy Gould for helpful discussions. We thank the anonymous referee, whose recommendations have improved the paper.

REFERENCES

- Alcock C. et al., 2001, *Nat*, 414, 617
- An J. H. et al., 2002, *ApJ*, 572, 521
- Barry R. et al., 2011, in Shaklan S., ed., *Proc. SPIE*, Vol. 8151, *Techniques and Instrumentation for Detection of Exoplanets V*. SPIE, Bellingham, 81510L
- Batalha N. M. et al., 2010, *ApJ*, 713, L109
- Batalha N. M. et al., 2013, *ApJS*, 204, 24
- Beaulieu J.-P. et al., 2006, *Nat*, 439, 437
- Beaulieu J. P. et al., 2008, preprint (arXiv:0808.0005)
- Beaulieu J. P. et al., 2010, in Coudé Du Foresto V., Gelino D. M., Ribas I., eds, *ASP Conf. Ser. Vol. 430, EUCLID: Dark Universe Probe and Microlensing Planet Hunter*. Astron. Soc. Pac., San Francisco, p. 266
- Beaulieu J.-P., Bennett D. P., Kerins E., Penny M., 2011, in Sozzetti A., Lattanzi M. G., Boss A. P., eds, *Proc. IAU Symp. 276, Towards Habitable Earths with EUCLID and WFIRST*. Cambridge Univ. Press, Cambridge, p. 349
- Beletic J. W. et al., 2008, in Dorn D. A., Holland A. H., eds, *SPIE Conf. Ser. Vol. 7021, High Energy, Optical, and Infrared Detectors for Astronomy III*. SPIE, Bellingham, 70210H
- Bennett D. P., 2004, in Beaulieu J., Lecavelier Des Etangs A., Terquem C., eds, *ASP Conf. Ser. Vol. 321, The Detection of Terrestrial Planets via Gravitational Microlensing: Space versus Ground-based Surveys*. Astron. Soc. Pac., San Francisco, p. 59
- Bennett D. P., Rhie S. H., 1996, *ApJ*, 472, 660
- Bennett D. P., Rhie S. H., 2002, *ApJ*, 574, 985
- Bennett D. P., Anderson J., Gaudi B. S., 2007, *ApJ*, 660, 781
- Bennett D. P. et al., 2008, *ApJ*, 684, 663
- Bennett D. P. et al., 2009, *Astro2010: The Astronomy and Astrophysics Decadal Survey*, Science White Papers, no. 18, preprint (arXiv:0902.3000)
- Bennett D. P. et al., 2010a, preprint (arXiv:1012.4486)
- Bennett D. P. et al., 2010b, *ApJ*, 713, 837
- Bennett D. P. et al., 2012, *ApJ*, 757, 119
- Bergeron P., Wesemael F., Beauchamp A., 1995, *PASP*, 107, 1047
- Bienayme O., Robin A. C., Creze M., 1987, *A&A*, 180, 94
- Blandford R. D. et al., 2010, *New Worlds, New Horizons in Astronomy and Astrophysics*. National Academies Press, Washington D.C.
- Bonfils X. et al., 2013, *A&A*, 549, A109
- Boss A. P., 1997, *Sci*, 276, 1836

- Boss A. P., 2006, *ApJ*, 644, L79
- Boss A. P., 2011, *ApJ*, 731, 74
- Calchi Novati S., de Luca F., Jetzer P., Mancini L., Scarpetta G., 2008, *A&A*, 480, 723
- Cameron A. G. W., 1978, *Moon Planets*, 18, 5
- Cassan A. et al., 2012, *Nat*, 481, 167
- Chabrier G., 1999, *ApJ*, 513, L103
- Clanton C., Beichman C., Vasisht G., Smith R., Gaudi B. S., 2012, *PASP*, 124, 700
- Cropper M. et al., 2010, in Oschmann J. M., Clampin M. C., MacEwen H. A., eds, *Proc. SPIE Vol. 7731, Space Telescopes and Instrumentation 2010: Optical, Infrared, and Millimeter Wave*. SPIE, Bellingham, 77311J
- Cumming A., Butler R. P., Marcy G. W., Vogt S. S., Wright J. T., Fischer D. A., 2008, *PASP*, 120, 531
- Cutri R. M. et al., 2003, 2MASS All Sky Catalog of Point Sources. NASA/IPAC Infrared Science Archive
- Dominik M., 1998, *A&A*, 333, L79
- Dominik M., 2006, *MNRAS*, 367, 669
- Dominik M., 2011, *MNRAS*, 411, 2
- Dressler A. et al., 2012, National Research Council Report of the Panel on Implementing Recommendations from the New Worlds, New Horizons Decadal Survey. The National Academies Press, Washington D.C.
- Einasto J., 1979, in Burton W. B., ed., *Proc. IAU Symp. 84, Galactic Mass Modeling*. D. Reidel Publ. Co., Dordrecht, p. 451
- Fixsen D. J., Offenberger J. D., Hanisch R. J., Mather J. C., Nieto-Santesteban M. A., Sengupta R., Stockman H. S., 2000, *PASP*, 112, 1350
- Freudenreich H. T., 1998, *ApJ*, 492, 495
- Gaudi B. S., Bennett D. P., Boden A. F., Forum 2008 Microlensing Committee E., 2009, *BAAS*, 41, 310.05
- Gautier T. N., III et al., 2012, *ApJ*, 749, 15
- Girardi L., Bertelli G., Bressan A., Chiosi C., Groenewegen M. A. T., Marigo P., Salasnich B., Weiss A., 2002, *A&A*, 391, 195
- Goldreich P., Tremaine S., 1980, *ApJ*, 241, 425
- Gould A., 1992, *ApJ*, 392, 442
- Gould A., 2000, *ApJ*, 542, 785
- Gould A., 2008, *ApJ*, 681, 1593
- Gould A., Gauchetel C., 1997, *ApJ*, 477, 580
- Gould A., Loeb A., 1992, *ApJ*, 396, 104
- Gould A. et al., 2010, *ApJ*, 720, 1073
- Green J. et al., 2011, preprint (arXiv:1108.1374)
- Green J. et al., 2012, preprint (arXiv:1208.4012)
- Griest K., Safizadeh N., 1998, *ApJ*, 500, 37
- Hamadache C. et al., 2006, *A&A*, 454, 185
- Han C., Chung S.-J., Kim D., Park B.-G., Ryu Y.-H., Kang S., Lee D. W., 2004, *ApJ*, 604, 372
- Hayashi C., 1981, *Prog. Theor. Phys. Suppl.*, 70, 35
- Haywood M., Robin A. C., Creze M., 1997, *A&A*, 320, 440
- Holman M. J. et al., 2010, *Sci*, 330, 51
- Holtzman J. A., Watson A. M., Baum W. A., Grillmair C. J., Groth E. J., Light R. M., Lynds R., O'Neil E. J., Jr, 1998, *AJ*, 115, 1946
- Howard A. W. et al., 2012, *ApJS*, 201, 15
- Ida S., Lin D. N. C., 2004, *ApJ*, 604, 388
- Ida S., Lin D. N. C., 2008, *ApJ*, 685, 584
- Johnson J. A. et al., 2010, *PASP*, 122, 149
- Kerins E., Robin A. C., Marshall D. J., 2009, *MNRAS*, 396, 1202
- Kim S. et al., 2010, in Stepp L., Gilmozzi R., Hall H., eds, *SPIE Conf. Ser. Vol. 7733, Ground-based and Airborne Telescopes III*. SPIE, Bellingham, 77333F
- Kozłowski S., Woźniak P. R., Mao S., Wood A., 2007, *ApJ*, 671, 420
- Kuiper G. P., 1951, *Proc. Natl. Acad. Sci.*, 37, 1
- Laureijs R. et al., 2011, preprint (arXiv:1110.3192)
- Leinert C. et al., 1998, *A&AS*, 127, 1
- Lissauer J. J., 1987, *Icarus*, 69, 249
- Lissauer J. J. et al., 2011, *ApJS*, 197, 8
- Lunine J. I. et al., 2008, *Astrobiology*, 8, 875
- Mao S., 2008, preprint (arXiv:0811.0441)
- Mao S., Paczyński B., 1991, *ApJ*, 374, L37
- Mao S., Paczyński B., 1996, *ApJ*, 473, 57
- Marshall D. J., Robin A. C., Reylé C., Schultheis M., Picaud S., 2006, *A&A*, 453, 635
- Masset F., Snellgrove M., 2001, *MNRAS*, 320, L55
- Mayor M. et al., 2011, preprint (arXiv:1109.2497)
- Mizuno H., 1980, *Prog. Theor. Phys.*, 64, 544
- Mordasini C., Alibert Y., Benz W., 2009a, *A&A*, 501, 1139
- Mordasini C., Alibert Y., Benz W., Naef D., 2009b, *A&A*, 501, 1161
- Nagasawa M., Ida S., Bessho T., 2008, *ApJ*, 678, 498
- Paczynski B., 1996, *ARA&A*, 34, 419
- Peale S. J., 2003, *AJ*, 126, 1595
- Pejcha O., Heyrovský D., 2009, *ApJ*, 690, 1772
- Peña Ramírez K., Béjar V. J. S., Zapatero Osorio M. R., Petr-Gotzens M. G., Martín E. L., 2012, *ApJ*, 754, 30
- Penny M. T., 2011, PhD thesis, Univ. Manchester
- Penny M. T., Mao S., Kerins E., 2011, *MNRAS*, 412, 607
- Picaud S., Robin A. C., 2004, *A&A*, 428, 891
- Popowski P. et al., 2005, *ApJ*, 631, 879
- Refregier A., 2009, *Exp. Astron.*, 23, 17
- Refregier A., Amara A., Kitching T. D., Rassat A., Scaramella R., Weller J., Euclid Imaging Consortium f. t., 2010, preprint (arXiv:1001.0061)
- Reylé C., Robin A. C., 2001, *A&A*, 373, 886
- Reylé C., Marshall D. J., Robin A. C., Schultheis M., 2009, *A&A*, 495, 819
- Robin A., Creze M., 1986, *A&A*, 157, 71
- Robin A. C., Reylé C., Derrière S., Picaud S., 2003, *A&A*, 409, 523
- Robin A. C., Marshall D. J., Schultheis M., Reylé C., 2012, *A&A*, 538, A106
- Safronov V. S., 1969, *Evolutsiia doplanetnogo oblaka* (English transl.: Evolution of the Protoplanetary Cloud and Formation of Earth and the Planets. NASA Tech. Transl. F-677, Israel Sci. Transl., Jerusalem, 1972)
- Saito R. K. et al., 2012, *A&A*, 537, A107
- Schaller G., Schaerer D., Meynet G., Maeder A., 1992, *A&AS*, 96, 269
- Schweitzer M. et al., 2010, in Oschmann J., Clampin M., MacEwen H., eds, *Proc. SPIE Vol. 7731, Space Telescopes 2010: Optical, Infrared and Millimeter Wave*. SPIE, Bellingham, 77311K
- Skowron J. et al., 2011, *ApJ*, 738, 87
- Smith M. C., Belokurov V., Evans N. W., Mao S., An J. H., 2005, *MNRAS*, 361, 128
- Spergel D. N. et al., 2012, Report of the Panel on Implementing Recommendations from the New Worlds, New Horizons Decadal Survey. National Academies Press, Washington D.C.
- Stevenson D. J., Lunine J. I., 1988, *Icarus*, 75, 146
- Sumi T., 2010, in Coudé Du Foresto V., Gelino D. M., Ribas I., eds, *ASP Conf. Ser. Vol. 430, MOA-II Microlensing Exoplanet Survey*. Astron. Soc. Pac., San Francisco, p. 225
- Sumi T. et al., 2006, *ApJ*, 636, 240
- Sumi T. et al., 2010, *ApJ*, 710, 1641
- Sumi T. et al., 2011, *Nat*, 473, 349
- Udalski A., 2011, in Bozza V., Calchi Novati S., Mancini L., Scarpetta G., eds, *XV International Conference on Gravitational Microlensing: Conference Book, Status of the OGLE-IV Survey*. p. 19, preprint (arXiv:1102.0452)
- Vanden Berg D. A., Bergbusch P. A., Dowler P. D., 2006, *ApJS*, 162, 375
- Veras D., Crepp J. R., Ford E. B., 2009, *ApJ*, 696, 1600
- Wambsganss J., 1997, *MNRAS*, 284, 172
- Ward W. R., 1997, *Icarus*, 126, 261
- Witt H. J., Mao S., 1994, *ApJ*, 430, 505
- Wright J. T. et al., 2011, *PASP*, 123, 412
- Yee J. C. et al., 2012, *ApJ*, 755, 102
- Yuan X., 2010, in Stepp L., Gilmozzi R., Hall H., eds, *Proc. SPIE Vol. 7733, Ground-based and Airborne Telescopes III*, SPIE, Bellingham, 77331V